

AD-A186 527

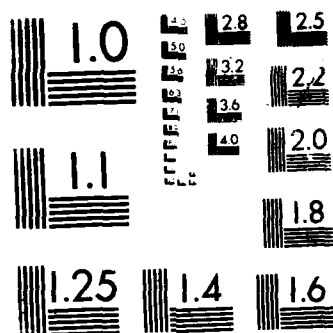
MINOR SCALE MICROWAVE TRANSMISSION EXPERIMENT AND
INVESTIGATION OF DUST I (U) SRI INTERNATIONAL MENLO
PARK CA D R MCDANIEL 30 SEP 86 DNA-TR-86-352-REV
DNA001-84-C-0391 E/G 20/1

1/1

UNCLASSIFIED

F/G 20/14

NL



MICROCOPY RESOLUTION TEST CHART
NATIONAL BUREAU OF STANDARDS 1963

AD-A186 527

4

DTIC FILE COPY

DNA-TR-86-352-~~100~~

MINOR SCALE MICROWAVE TRANSMISSION EXPERIMENT AND INVESTIGATION OF DUST INSTABILITY MECHANISMS

D. R. McDaniel
SRI International
333 Ravenswood Avenue
Menlo Park, CA 94025-3434

30 September 1986

Technical Report

DTIC
ELECTE
OCT 20 1987
S D

CONTRACT No. DNA 001-84-C-0391

Approved for public release;
distribution is unlimited.

THIS WORK WAS SPONSORED BY THE DEFENSE NUCLEAR AGENCY
UNDER RDT&E RMC CODE B3220844692 RQ RC 00025 25904D.

Prepared for
Director
DEFENSE NUCLEAR AGENCY
Washington, DC 20305-1000

87

10

8

002

Destroy this report when it is no longer needed. Do not return to sender.

PLEASE NOTIFY THE DEFENSE NUCLEAR AGENCY
ATTN: TITL, WASHINGTON, DC 20305 1000, IF YOUR
ADDRESS IS INCORRECT, IF YOU WISH IT DELETED
FROM THE DISTRIBUTION LIST, OR IF THE ADDRESSEE
IS NO LONGER EMPLOYED BY YOUR ORGANIZATION.



DISTRIBUTION LIST UPDATE

This mailer is provided to enable DNA to maintain current distribution lists for reports. We would appreciate your providing the requested information.

- ☐ Add the individual listed to your distribution list.
- ☐ Delete the cited organization/individual.
- ☐ Change of address.

NAME: _____

ORGANIZATION: _____

OLD ADDRESS

CURRENT ADDRESS

TELEPHONE NUMBER: () _____

SUBJECT AREA(s) OF INTEREST:

DNA OR OTHER GOVERNMENT CONTRACT NUMBER: _____

CERTIFICATION OF NEED-TO-KNOW BY GOVERNMENT SPONSOR (if other than DNA):

SPONSORING ORGANIZATION: _____

CONTRACTING OFFICER OR REPRESENTATIVE: _____

SIGNATURE: _____

CUT HERE AND RETURN



Director
Defense Nuclear Agency
ATTN: [REDACTED] TITL
Washington, DC 20305-1000

Director
Defense Nuclear Agency
ATTN: [REDACTED] TITL
Washington, DC 20305-1000

UNCLASSIFIED
SECURITY CLASSIFICATION OF THIS PAGE

ADA186527

REPORT DOCUMENTATION PAGE				
1a. REPORT SECURITY CLASSIFICATION UNCLASSIFIED		1b. RESTRICTIVE MARKINGS		
2a. SECURITY CLASSIFICATION AUTHORITY N/A since Unclassified		3. DISTRIBUTION/AVAILABILITY OF REPORT Approved for public release; distribution is unlimited.		
2b. DECLASSIFICATION/DOWNGRADING SCHEDULE N/A since Unclassified				
4. PERFORMING ORGANIZATION REPORT NUMBER(S) SRI Project 7802		5. MONITORING ORGANIZATION REPORT NUMBER(S) DNA-TR-86-352- 		
6a. NAME OF PERFORMING ORGANIZATION SRI International		6b. OFFICE SYMBOL (if applicable)	7a. NAME OF MONITORING ORGANIZATION Director Defense Nuclear Agency	
6c. ADDRESS (City, State, and ZIP Code) 333 Ravenswood Avenue Menlo Park, California 94025-3434		7b. ADDRESS (City, State, and ZIP Code) Washington, DC 20305-1000		
8a. NAME OF FUNDING/SPONSORING ORGANIZATION		8b. OFFICE SYMBOL (if applicable) RAAE/Emmes	9. PROCUREMENT INSTRUMENT IDENTIFICATION NUMBER DNA 001-84-C-0391	
8c. ADDRESS (City, State, and ZIP Code)		10. SOURCE OF FUNDING NUMBERS		
		PROGRAM ELEMENT NO. 62715H	PROJECT NO. RQ	TASK NO. RC WORK UNIT ACCESSION NO. DH251307
11. TITLE (Include Security Classification) MINOR SCALE MICROWAVE TRANSMISSION EXPERIMENT AND INVESTIGATION OF DUST INSTABILITY MECHANISMS				
12. PERSONAL AUTHOR(S) McDaniel, Dan R.				
13a. TYPE OF REPORT Technical		13b. TIME COVERED FROM 840901 TO 860801	14. DATE OF REPORT (Year, Month, Day) 860930	15. PAGE COUNT 54
16. SUPPLEMENTARY NOTATION This work was sponsored by the Defense Nuclear Agency under RDT&E RMC Code B3220844692 RQ RC 00025 25904D.				
17. COSATI CODES			18. SUBJECT TERMS (Continue on reverse if necessary and identify by block number) Nuclear Effects Turbulence Theory RF Propagation	
FIELD	GROUP	SUB-GROUP		
18	3			
20	4			
19. ABSTRACT (Continue on reverse if necessary and identify by block number) An experiment was planned but not executed for a DNA high-explosive test that would resolve problems encountered in the application of conventional turbulence theory to dust effects. This experiment would have involved X-band rf transmissions through the turbulent pedestal, by measuring angle-of-arrival and changes in signal amplitude and phase caused by dust loading. These data would have been used to establish the spatial and temporal parameters of the dust-induced variations. Because of the difference between observed turbulence and that predicted by the Kolmogorov turbulence theory, plus the excessive dust-pedestal rise rates compared with the code predictions, a study of intrinsic mechanisms for toroidal instabilities was carried out. The study focussed primarily on vortex formation, trajectories, and				
20. DISTRIBUTION/AVAILABILITY OF ABSTRACT <input type="checkbox"/> UNCLASSIFIED/UNLIMITED <input checked="" type="checkbox"/> SAME AS RPT <input type="checkbox"/> DTIC USERS			21. ABSTRACT SECURITY CLASSIFICATION UNCLASSIFIED	
22a. NAME OF RESPONSIBLE INDIVIDUAL Sandra E. Young			22b. TELEPHONE (Include Area Code) (202) 325-7042	22c. OFFICE SYMBOL DNA/CSTI

DD FORM 1473, 84 MAR

83 APR edition may be used until exhausted.
All other editions are obsolete.

SECURITY CLASSIFICATION OF THIS PAGE

UNCLASSIFIED

19. ABSTRACT (Continued)

— circumferential instabilities, which are set forth as the principal mechanism for formation of the ring-wave-cell structure observed during DIRECT COURSE.

PREFACE

We wish to acknowledge Drs. R. J. Swigart and W.C.L. Shih of Physical Research, Inc., and Dr. Sheila E. Widnall of MIT for their work on the instability mechanism investigation reported in Section 3 of this report. Also, the contribution to the overall project of Dr. Alan A. Burns of Vista Research, Inc., formerly of SRI International, is gratefully acknowledged.



Accession For	
NTIS	CRA&I <input checked="" type="checkbox"/>
DTIC	TAB <input type="checkbox"/>
Unpublished	<input type="checkbox"/>
Justification	
By _____	
Distribution /	
Availability codes	
Dist	Acad. and/or Special
A-1	

CONVERSION TABLE

Conversion factors for U.S. Customary to metric (SI) units of measurement

MULTIPLY TO GET	BY	TO GET DIVIDE
angstrom	1.000 000 X E -10	meters (m)
atmosphere (normal)	1 013 25 X E +2	kilo pascal (kPa)
bar	1.000 000 X E +2	kilo pascal (kPa)
barn	1.000 000 X E -28	meter ² (m ²)
British thermal unit (thermochemical)	1.054 350 X E +3	joule (J)
calorie (thermochemical)	4.184 000	joule (J)
cal (thermochemical).cm ²	4.184 000 X E -2	mega joule/m ² (MJ/m ²)
curie	3 700 000 X E +1	*giga becquerel (GBq)
degree (angle)	1.745 329 X E -2	radian (rad)
degree Fahrenheit	$t_x = (t^{\circ}f + 459.67)/1.8$	degree kelvin (K)
electron volt	1.602 19 X E -19	joule (J)
erg	1.000 000 X E -7	joule (J)
erg/second	1.000 000 X E -7	watt (W)
foot	3.048 000 X E -1	meter (m)
foot-pound-force	1.355 818	joule (J)
gallon (U.S. liquid)	3.785 412 X E -3	meter ³ (m ³)
inch	2.540 000 X E -2	meter (m)
jerk	1.000 000 X E +9	joule (J)
joule/kilogram (J/kg) (radiation dose absorbed)	1.000 000	Gray (Gy)
kilotons	4.193	terajoules
kip (1000 lbf)	4.448 222 X E +3	newton (N)
kip. inch ² (ksi)	6.894 757 X E +3	kilo pascal (kPa)
knap	1.000 000 X E +2	newton-second/m ² (N-s/m ²)
micron	1.000 000 X E -6	meter (m)
mil	2.540 000 X E -5	meter (m)
mile (international)	1.609 344 X E +3	meter (m)
ounce	2.834 952 X E -2	kilogram (kg)
pound-force (lbs avoirdupois)	4.448 222	newton (N)
pound-force/ inch	1.129 348 X E -1	newton-meter (N-m)
pound-force/ inch	1.751 268 X E +2	newton/meter (N/m)
pound-force/foot ²	4.798 026 X E -2	kilo pascal (kPa)
pound-force/ inch ² (psi)	6.894 757	kilo pascal (kPa)
pound-mass (lbm avoirdupois)	4.535 924 X E -1	kilogram (kg)
pound-mass-foot ² (moment of inertia)	4.214 011 X E -2	kilogram-meter ² (kg-m ²)
pound-mass foot ³	1.401 346 X E +1	kilogram/meter ³ (kg-m ³)
rad (radiation dose absorbed)	1.000 000 X E -2	*Gray (Gy)
roentgen	2.579 760 X E -4	coulomb/kilogram (C/kg)
shake	1.000 000 X E -8	second (s)
slug	1.459 390 X E +1	kilogram (kg)
torr (mm Hg, 0° C)	1.333 22 X E -1	kilo pascal (kPa)

*The becquerel (Bq) is the SI unit of radioactivity; 1 Bq = 1 event/s.

**The Gray (Gy) is the SI unit of absorbed radiation.

TABLE OF CONTENTS

Section	Page
PREFACE	iii
CONVERSION TABLE	iv
LIST OF ILLUSTRATIONS	vi
1 INTRODUCTION	1
2 THE MINOR SCALE EXPERIMENT	2
3 INVESTIGATION OF INSTABILITY MECHANISMS.	6
3.1 Background	6
3.2 Vortex Formation, Motion, and Circumferen- tial Stability	6
3.2.1 The DIRECT COURSE Event	6
3.2.2 Mechanism for Vortex Formation	7
3.2.3 Mechanism for Dust Pedestal Cellular Structure	20
4 LIST OF REFERENCES	39

LIST OF ILLUSTRATIONS

Figure		Page
1	MINOR SCALE rf transmission experiment-- Perspective of layout (27 July 1984)	4
2	Photograph of DIRECT COURSE event showing dust pedestal ring 15 s after detonation.	8
3	Dimensions of the DIRECT COURSE cloud pedestal. . .	9
4	Results of HULL calculations for DIRECT COURSE velocity field showing formation and persistence of low-lying far-radius vortex field	10
5	Diagrams of triple-point mechanism	13
6	Extreme incidence angle, ω_e , beyond which regular reflections cannot occur, as a function of shock strength $\xi \equiv p_1/p_2$	14
7	Definition of angle, ω , of blast-shock intersection with ground plane	15
8	Angle of blast-shock intersection vs distance along ground	15
9	Dual bursts generating shock intersection equiva- lent to ground reflection of single burst	16
10	Bow-shock radius vs time for DIRECT COURSE event as calculated by the HULL code	17
11	Triple-Point trajectory for DIRECT COURSE event as calculated by the HULL code	17
12	Results of HULL calculations for DIRECT COURSE pressure field at 100, 250, and 500 ms showing development of triple point	18
13	Velocity difference across triple-point slipstream	19
14	History of the triple-point radial location	19

Figure		Page
15	Overhead photograph of DIRECT COURSE event 4.5 s after detonation showing circumferential cellular structure of dust pedestal	21
16	Ring-vortex periodic waves as observed in the laboratory by pulsing air through a sharp-edged orifice	23
17	Ring-vortex nomenclature	24
18	Results of vortex-ring circumferential stability analysis	24
19	Coordinate system for vortex sheet calculations . .	28
20	Equivalent core for vortex sheet rollup	28
21	Calculated vortex position as function of time, $t = 0$ to 4 s	36
22	Calculated vortex position as function of time, $t = 0$ to 6 s	36
23	Calculated vortex position as function of time, $t = 0$ to 8 s	37
24	Vortex sheet velocity field, $t = 0$ s	37
25	Vortex sheet velocity field, $t = 3$ s	38
26	Vortex sheet velocity field, $t = 8$ s	38

SECTION I

INTRODUCTION

Surface dust that has been scoured and lofted over a wide area surrounding a near-surface nuclear detonation can have potentially severe, deleterious effects on communications and sensor systems. Consequently, the effects of dust in nuclear sweep-up and dust-pedestal clouds are incorporated in the nuclear-effects codes. However, many of the assumptions concerning both the mean properties of the dust distribution and the fluctuations in refractive index at microwave frequencies produced by irregularities in dust density have not been verified experimentally, and, in at least some instances, appear to be erroneous or inaccurate. SRI International, under Defense Nuclear Agency (DNA) and U.S. Army Ballistic Missile Defense Advanced Technology Center (BMDATC) sponsorship (Contract DNA 001-83-C-0203), fielded an experiment to measure the rf effects produced by the dust pedestal lofted by the DIRECT COURSE high explosive detonation. In particular, the results from those measurements, although incomplete, have pointed out apparent deficiencies in the application of conventional turbulence theory to dust effects.

In this project, we put forward a plan to complete the DIRECT COURSE measurement program and to resolve the dust effects issues that have recently emerged. The planned work was designed to exploit the MINOR SCALE test, which took place in mid-June 1985. The planned microwave experiment was cancelled so we initiated a study of intrinsic mechanisms for toroidal instabilities in the dust pedestal. This study was carried out by Physical Research, Inc., under subcontract to SRI International.

SECTION 2

THE MINOR SCALE EXPERIMENT

The primary objectives of the planned experiment were to

- Make spaced-antenna/angle-of-arrival measurements for signals passing along a number of paths at various elevations above the surface that could be used to establish the parameters of dust-induced signal fluctuations or "turbulence" and the spatial variation thereof
- Measure the changes in signal amplitude and phase caused by the dust loading, then estimate the magnitude of the loading
- Complete and extend the DIRECT COURSE measurements.

SRI planned to make these measurements with the rf transmission technique using three X-band (8086-MHz) transmitters and nine receivers at three locations--thereby providing nine different paths to penetrate the dust cloud. We planned to modify the 9086-MHz part of the equipment built for DNA and BMDATC for the DIRECT COURSE transmission experiment for this purpose. Support would be needed from FCDNA for testbed construction and installation, aircraft tracking, and frequency allocation approvals.

There were to be two phases to the effort. The first involved the necessary preliminary activities of detailed experimental planning, design, and coordination, plus construction of items (e.g., antenna supports) to be delivered to the test bed well before the main fielding effort. Part of this activity included attending the Project Officers Meetings scheduled by FCDNA and providing support to FCDNA. The second phase involved the preparation of the equipment and the fielding and execution of the experiment. An extensive data-analysis effort was not

part of the program; rather, a quick-look analysis was proposed, using some of the software developed for the DIRECT COURSE data analysis, primarily to assess the data quality. A future effort to reduce the MINOR SCALE data and to analyze those results (incorporating the DIRECT COURSE results as well) was to be proposed following successful accomplishment of the experiment.

SRI planned to reconfigure part of the equipment assembled for the DIRECT COURSE transmission experiment (under Contract DNA 001-83-C-0203) to provide for one airborne and two ground-based transmitters and nine receiver channels. Each receiver channel would accommodate all three transmitter signals by means of frequency multiplexing (the ground-based transmitters would be slightly offset in frequency from each other and from the airborne transmitter). Figure 1 is a perspective view of the experimental layout, which was designed to exploit the precursed dusty radial on a noninterference basis.

A formal technical support plan (TSP) and a program document were submitted to Field Command DNA, who designated this experiment as MINOR SCALE Experiment Number 8540. Project personnel attended the Project Officers Meetings held during the weeks of 24 September and 26 November 1984. During these meetings, most of the details of the construction and logistical support requirements were finalized, and the preliminary layout of the experiment was established.

Work was begun on our task to reconfigure the equipment. At this point, we were informed that our experiment would not be included in MINOR SCALE, and that the remaining effort should be directed toward planning for future tests. Part of our subsequent activity was to prepare a TSP and a program document for the MISTY PICTURE HE event scheduled for Spring 1986. Both documents were submitted to DNA. The MISTY PICTURE event, however, has now been delayed until May 1987.

Much of our work has been directed toward designing an experiment to address the issues raised by the discrepancies between the results of our experiment for DIRECT COURSE and the theoretical expectations that

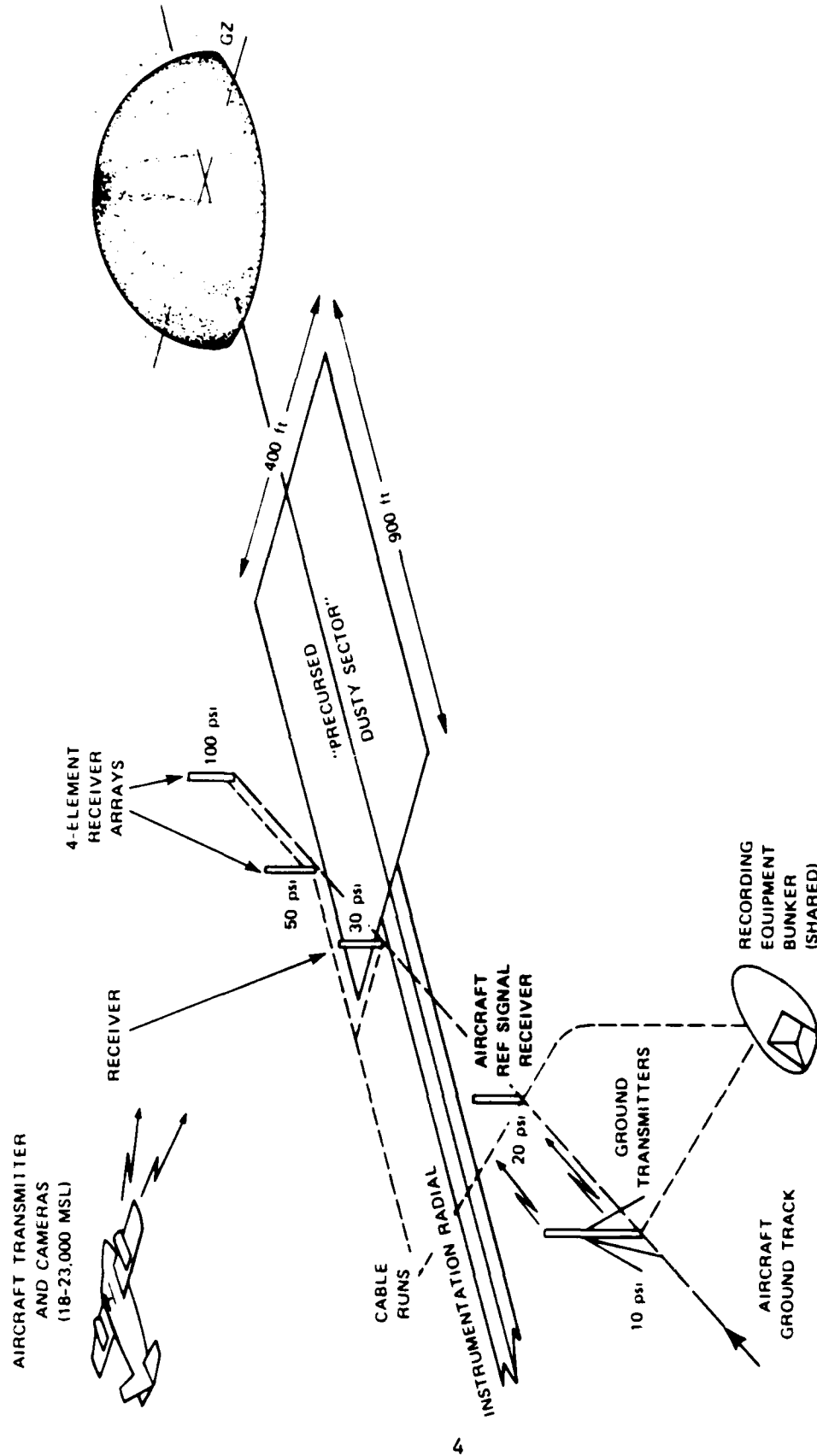


Figure 1. MINOR SCALE of transmission experiment—perspective of layout (27 July 1984).

are embodied in the nuclear-effects codes. The observed turbulence differed from that predicted by the Kolmogorov turbulence theory, and the dust-pedestal rise rate was far in excess of that inferred from the two-dimensional hydrodynamic codes (HULL code). The latter discrepancy appears to be caused by a three-dimensional instability in the pedestal region. It is a significant issue because it implies greater dust lofting and entrainment than predicted and is a mechanism for producing continued turbulence. As a result, we initiated a study of intrinsic mechanisms for toroidal instabilities. This is relevant because the initial condition before the instability sets in appears to be the thin, "reverse" torus near the surface, which is predicted by the hydrocode calculation for 1-MT nuclear height-of-burst (HOB) events. Section 3 of this report presents the results of this study.

SECTION 3

INVESTIGATION OF INSTABILITY MECHANISMS

3.1 BACKGROUND.

An in-depth investigation of the following possible dust-density irregularity production and dissipation mechanisms was carried out

- Conditions for Mach reflection
- Mechanism for vortex formation
- Vortex trajectory
- Vortex instabilities
- Post-shock-wave hydrodynamic instabilities
- Post-shock-wave convective instabilities.

This work reported in this chapter focuses principally on vortex formation, trajectories, and circumferential instabilities, which are set forth as the principal mechanism for formation of ring-wave cell structure. This structure was observed to form close to the ground during the DIRECT COURSE event. Post-shock-wave convective instability was also investigated as a possible mechanism for formation of the observed cellular structure.

3.2 VORTEX FORMATION, MOTION, AND CIRCUMFERENTIAL STABILITY.

3.2.1 The DIRECT COURSE Event.

DIRECT COURSE was a 600-ton yield, 50-m height-of-burst high-explosive event. The explosive utilized a mixture of ammonium nitrate and fuel oil (ANFO). Data recorded during the event included photographic coverage, dynamic and static pressure, hot-wire measurements (mean and fluctuating velocity and temperature components), dust-density levels, and electromagnetic-wave propagation characteristics.

In particular, photographic coverage revealed the formation of a "dust pedestal" ring (Figure 2), which was observed to form close to the ground shortly after detonation. The time history of the height and the radius of the ring for the first second after detonation as derived from our data is shown in Figure 3. Note that both the radius and height level off to constant values of about 200 m and 35 m, respectively, after about 0.5 s. In addition, hydrodynamic calculations using the HULL computer code reveal a ground-level vortex forming at about 1 s at a radial location of about 180 m, and persisting at that location through times as late as 15 s (Figure 4). Moreover, observation from above revealed a circumferential cellular structure in the dust pedestal consisting of about 30 cells, the formation of which is the main subject of the investigation carried out herein. The two primary candidates investigated to explain the dust pedestal cellular structure are ring vortex instabilities and convective cells (also known as Benard cells).

3.2.2 Mechanism for Vortex Formation.

Line and ring vortices form as a result of shear or swirl in flows, which may be caused by a variety of flow mechanisms; e.g., in the laboratory vortex rings are produced by pulsing a fluid through a sharp-edged circular orifice and the vortex forms due to the shearing motion of the fluid in the vicinity of the orifice edge, which causes the flow to roll up into a vortex ring. Early-time vortical toroidal motion within a rising buoyant thermal, however, develops because of the reverse flow toward the center of the thermal--as a result of inwardly-directed pressure gradients generated by passage of the blast shock wave.

Regardless of the formative mechanism, it must give rise to a shear-type velocity profile in order for a vortical flow to develop.



Figure 2. Photograph of DIRECT COURSE event showing dust pedestal ring 15 s after detonation.

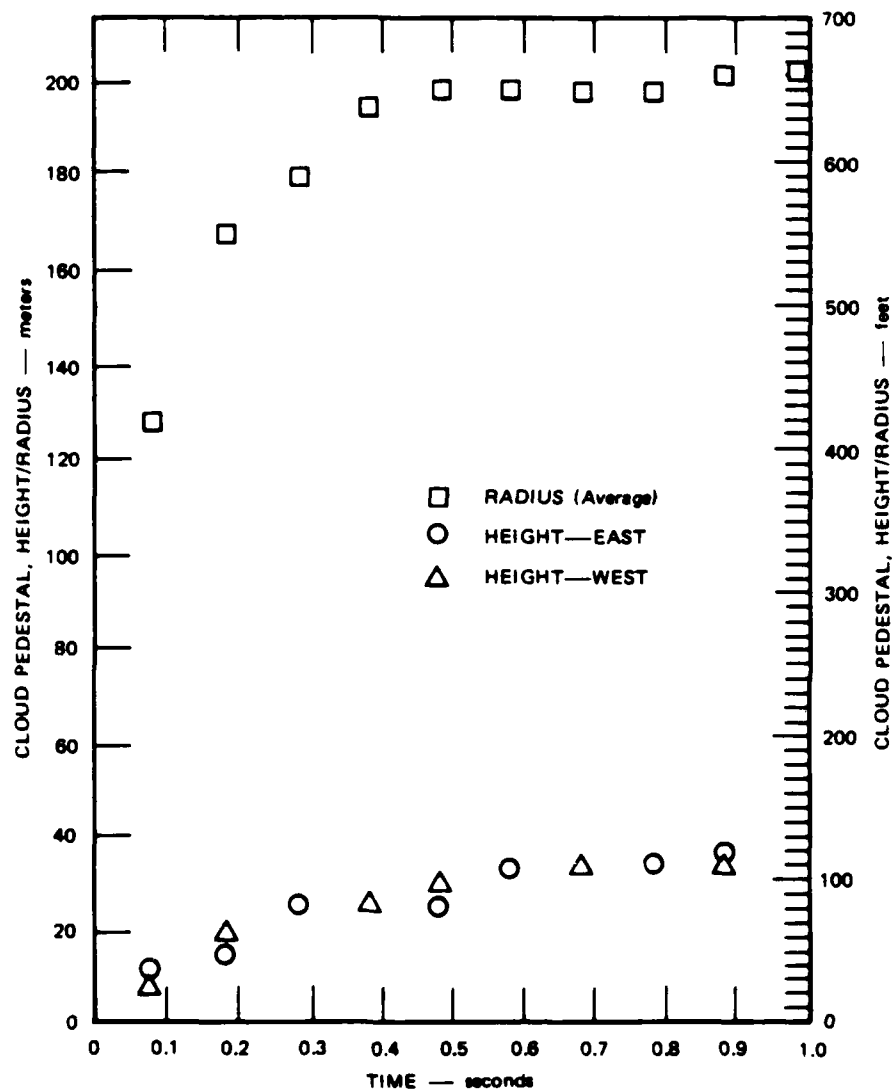


Figure 3. Dimensions of the DIRECT COURSE cloud pedestal.

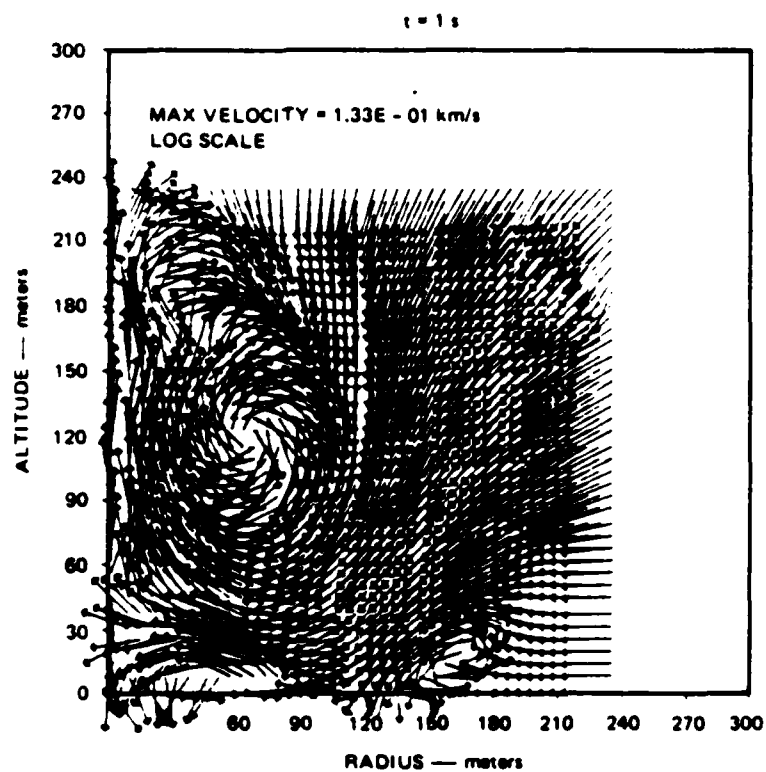
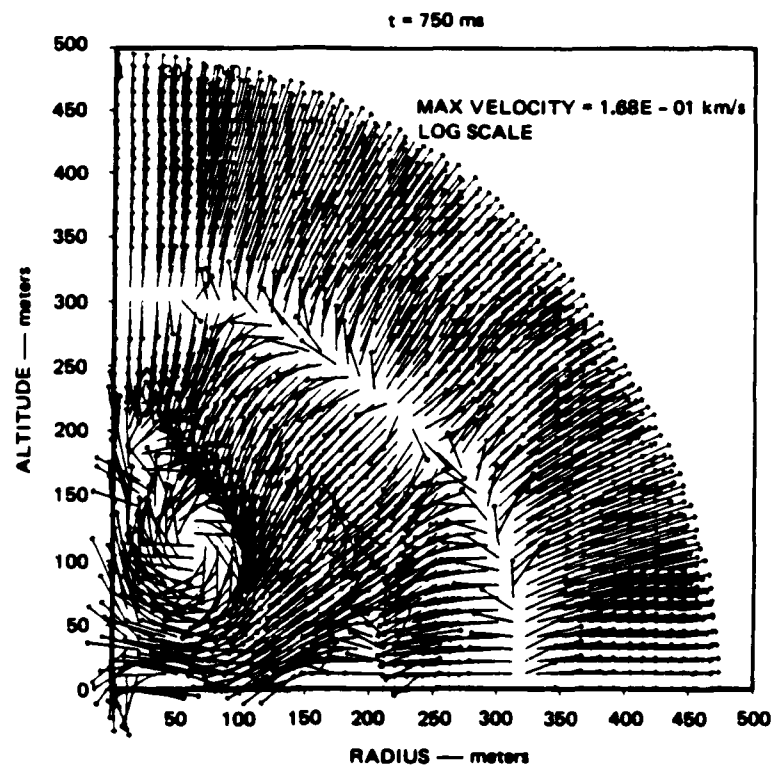


Figure 4. Results of HULL calculations for the DIRECT COURSE velocity field showing formation and persistence of the low-flying far-radius vortex field.

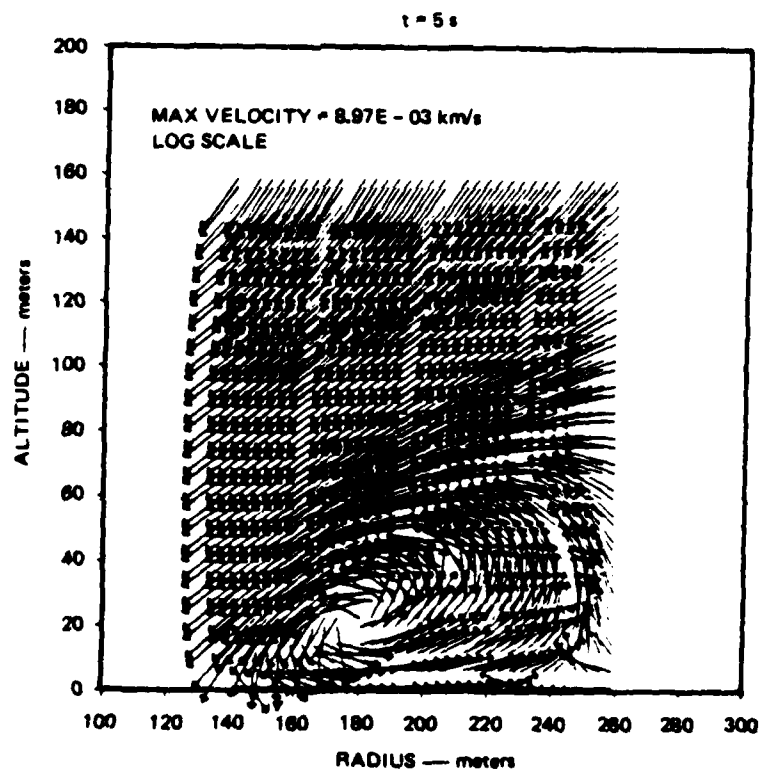
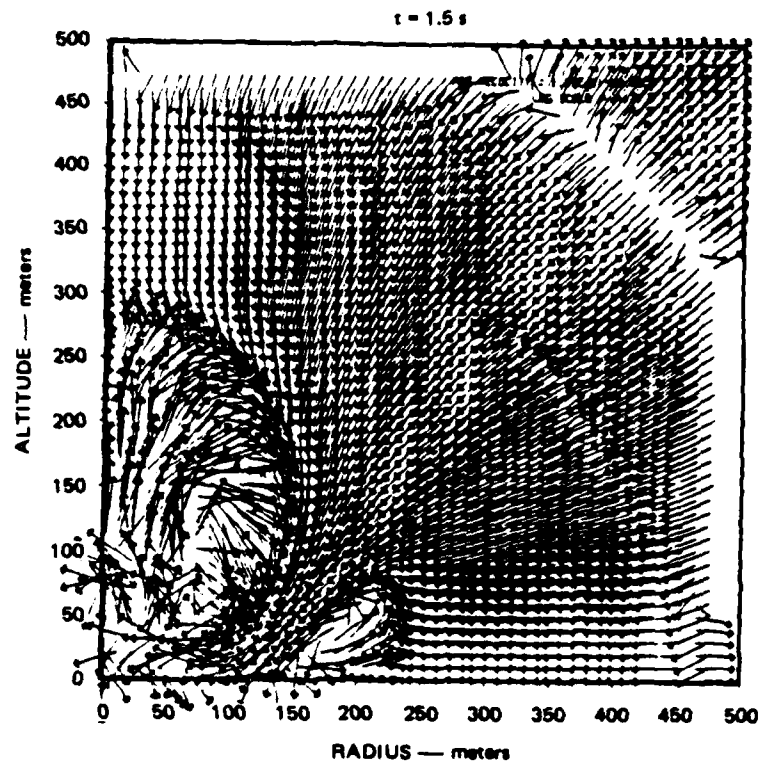


Figure 4. Results of HULL calculations for the DIRECT COURSE velocity field showing formation and persistence of the low-flying far-radius vortex field (Continued).

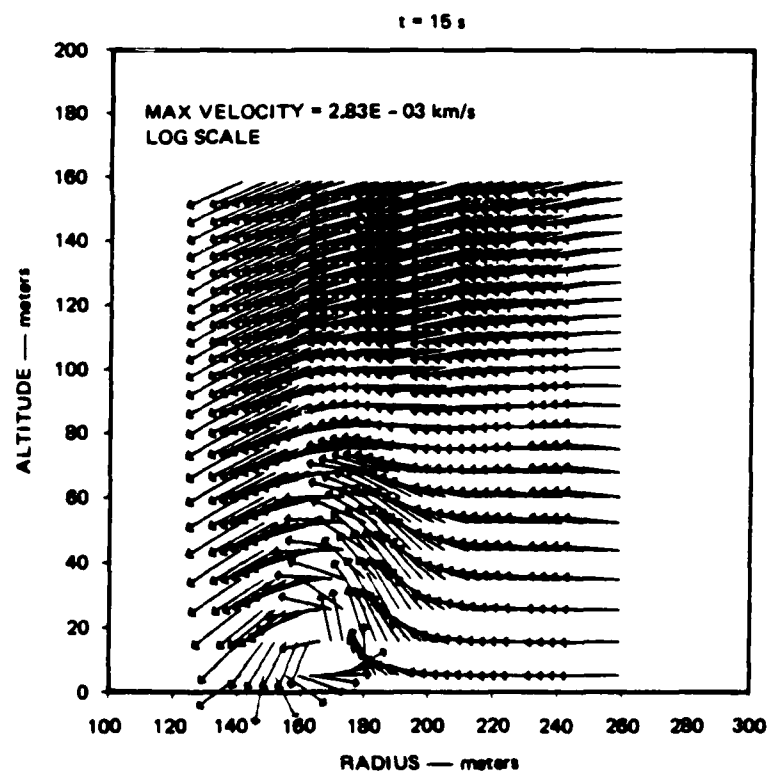
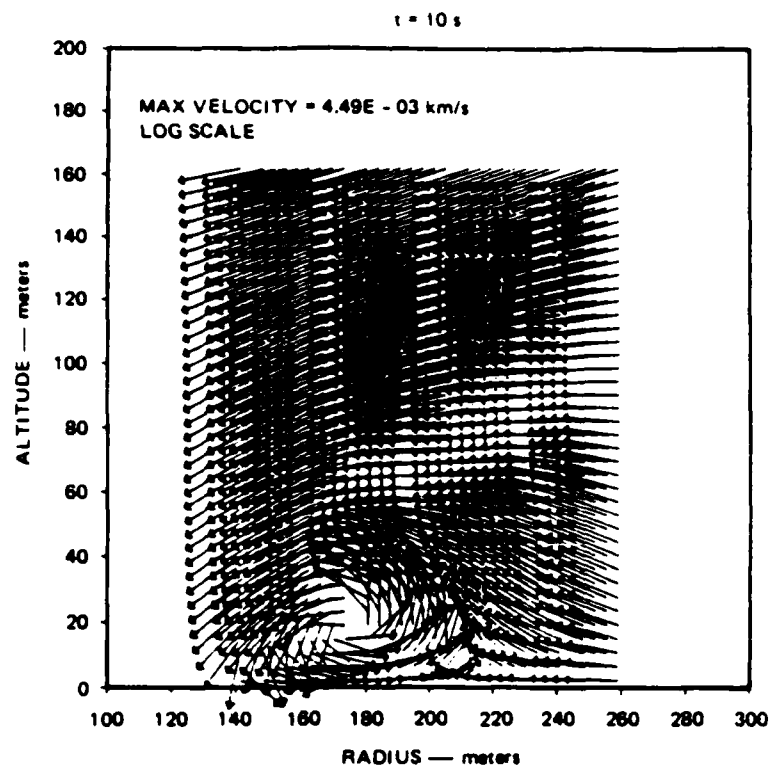


Figure 4. Results of HULL calculations for the DIRECT COURSE velocity field showing formation and persistence of the low-flying far-radius vortex field (Concluded).

One such mechanism is the presence of a "triple point," which occurs when a shock wave reflects off a surface and conditions are such that a regular reflection cannot occur, giving rise to a so-called Mach reflection (Figure 5; M = Mach number, p = pressure). The extreme incidence angle, ω_e , beyond which a regular reflection cannot occur, is shown in Figure 6 as a function of shock strength, $\xi \equiv p_1/p_2$, the reciprocal of the pressure ratio across the incident shock wave. Formation of a triple point gives rise to a slipstream [Figure 5(b)], which divides the downstream flow above and below the triple point. Because the flows in these two regions traverse different shock systems, the entropy and velocity are different on the upper and lower sides of the slipstream. The only quantities that are constant across the slipstream are the pressure and flow direction. This velocity difference (the "slip" in slipstream) occurs, in reality, across a very thin region of high-velocity gradients, which can be represented by a vortex sheet. It is this region of high-velocity gradients (high shear) that provides a possible formative mechanism for the ring-vortex explanation of the dust pedestal phenomenon observed in the DIRECT COURSE event.

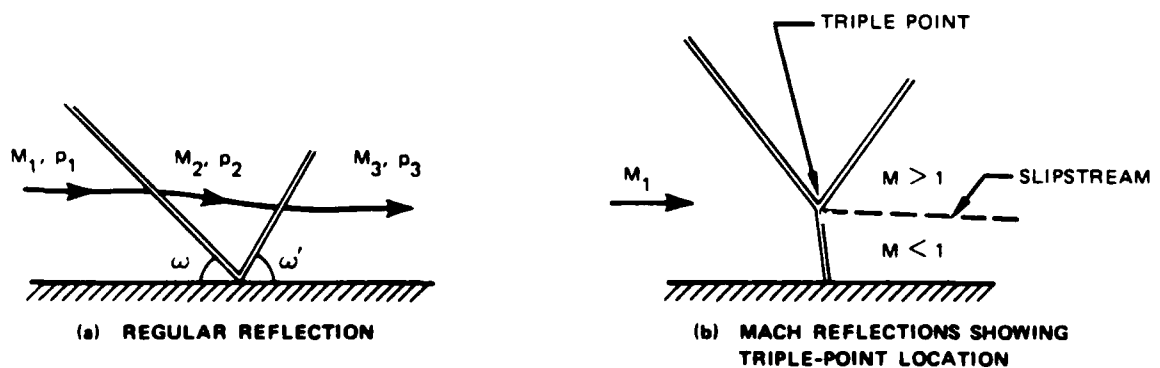


Figure 5. Diagrams of triple-point mechanism.

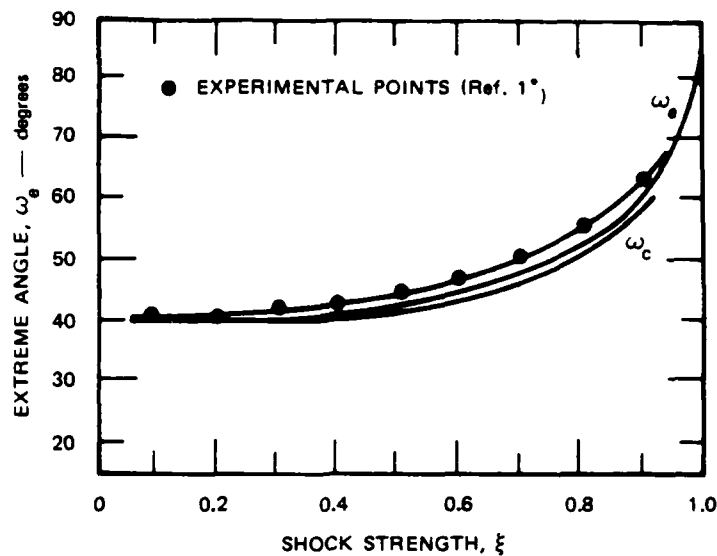


Figure 6. Extreme incidence angle, ω_e , beyond which regular reflections cannot occur as a function of shock strength $\xi \equiv p_1/p_2$.

To see at what radius along the ground the blast shock must be in order for the triple-point phenomenon to occur, the incidence angle, ω , is defined as the angle that the tangent to the expanding spherical blast shock wave at its ground intersection point makes with the ground plane (Figure 7). From Figure 6 note that, at early times (low values of shock strength, ξ), ω must be > 40 deg in order for a Mach reflection to occur. For the DIRECT COURSE blast shock centered at 50 m above the ground, this angle will occur at a radius of about 46 m (Figure 8) as obtained from HULL code calculations. Physically, this triple point is formed by the intersection of incident, reflected, and Mach reflection shocks. Under the assumption of perfect reflection at the ground (no energy absorption), the shock structure is equivalent to that generated by the intersection in the horizontal-symmetry plane of the spherical blast shocks. These shocks are created by two bursts of the same yield (detonating simultaneously) whose centers are separated by a distance twice that of the single burst above the ground (Figure 9). For the DIRECT COURSE event, plots of the bow-shock-radius temporal history

* References are listed in order of appearance at the end of this report.

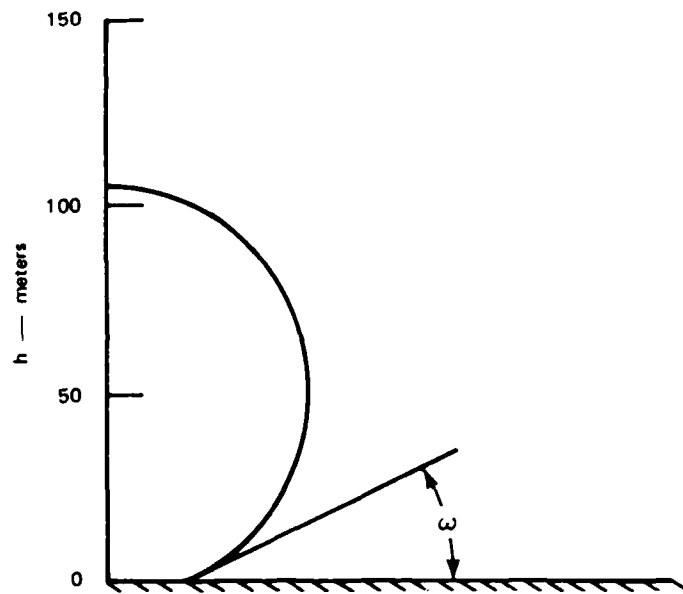


Figure 7. Definition of angle ω of blast-shock intersection with ground plane.

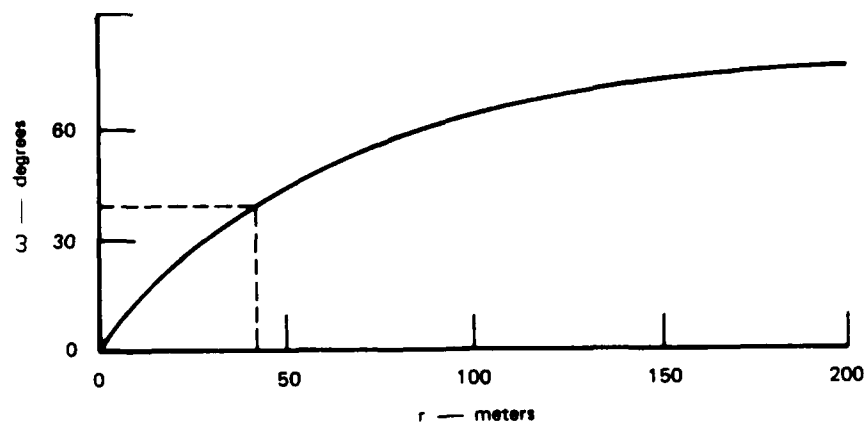


Figure 8. Angle of blast-shock intersection vs distance along ground.

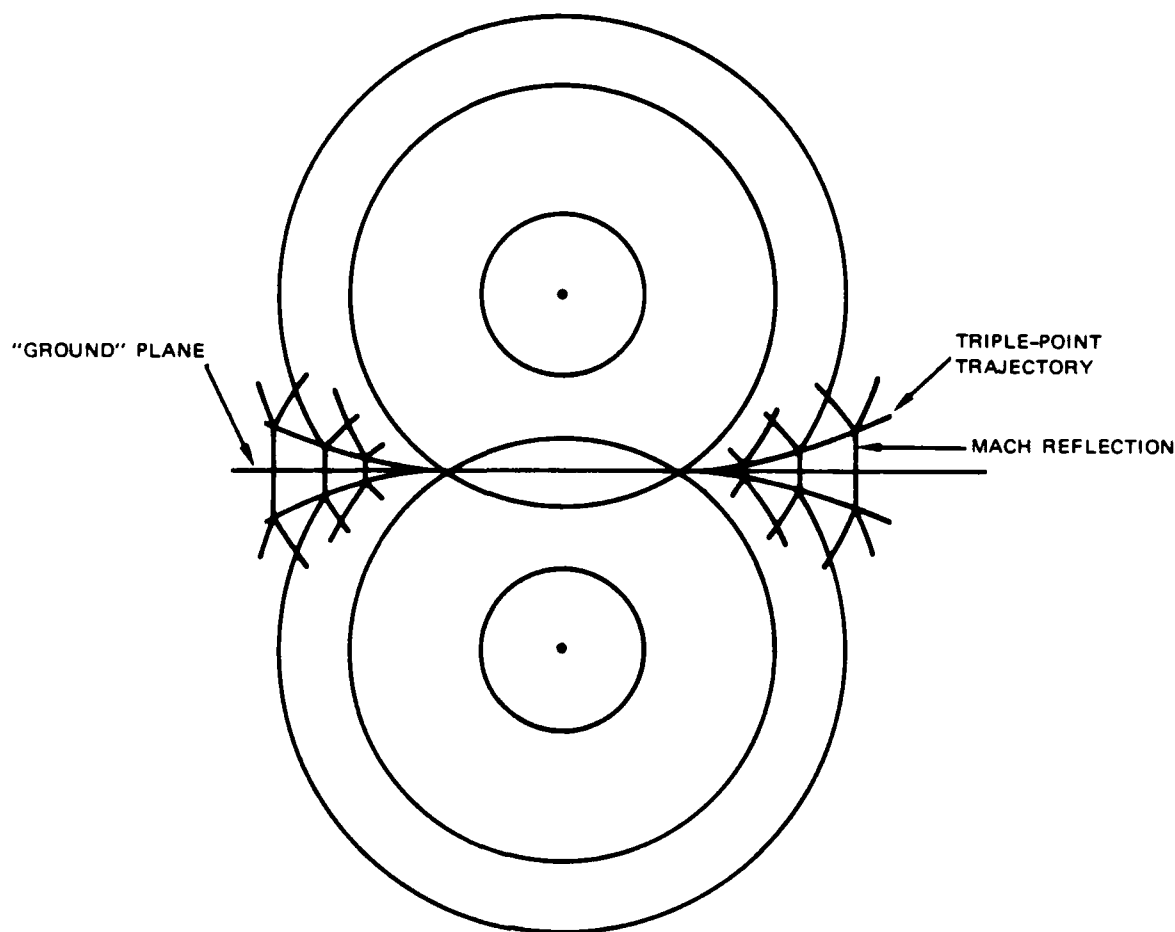


Figure 9. Dual bursts generating shock interaction equivalent to ground reflection of single burst.

and the triple-point trajectory (as calculated by S-Cubed using the HULL computer code) are shown in Figures 10 and 11. Typical HULL calculational results for pressure distribution, from which bow-shock radius and triple-point location are determined, are shown in Figure 12.

To determine whether the shear layer generated downstream of the triple point is a possible causative mechanism for the ring-vortex explanation of dust-pedestal formation, the velocity difference across the triple-point slipstream was considered, as shown in Figure 13, also based on HULL calculations. Note that this difference is a maximum at about 0.195 s, which yields a triple-point radius of 175 m, (see Figure 14). This is in substantial agreement with the dust-pedestal data (Figure 3), which show a radius of about 170 m at 0.195 s. Thus, a

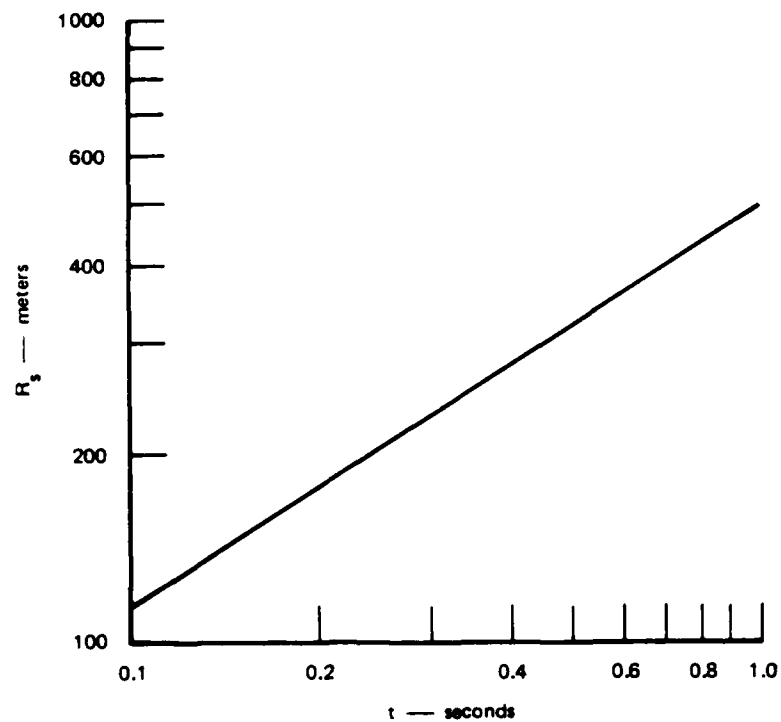


Figure 10. Bow shock radius vs time for DIRECT COURSE event as calculated by the HULL Code.

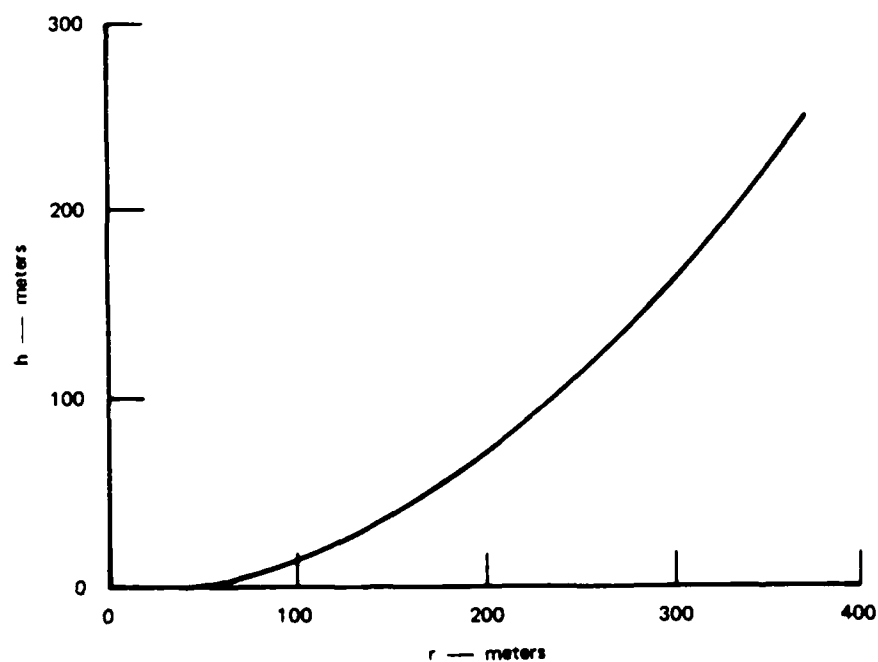


Figure 11. Triple-point trajectory for DIRECT COURSE event as calculated by the HULL Code.

CONTOUR SCALE

	DYNE/cm ²	kPa
2	8.000E + 05	80
3	1.600E + 06	160
4	2.400E + 06	240
5	3.200E + 06	320
6	4.000E + 06	400
7	4.800E + 06	480
8	5.600E + 06	560
9	6.400E + 06	640

MIN = 3.622E + 03 0.3622
MAX = 7.139E + 06 713.9

CONTOUR SCALE

	DYNE/cm ²	kPa
2	5.000E + 05	50
3	7.500E + 05	75
4	1.000E + 06	100
5	1.250E + 06	125
6	1.500E + 06	150
7	1.750E + 06	175
8	2.000E + 06	200
9	2.250E + 06	225

MIN = 4.229E + 05 42.29
MAX = 2.351E + 06 235.1

CONTOUR SCALE

	DYNE/cm ²	kPa
2	6.000E + 05	60
3	7.000E + 05	70
4	8.000E + 05	80
5	9.000E + 05	90
6	1.000E + 06	100
7	1.100E + 06	110
8	1.200E + 06	120
9	1.300E + 06	130
10	1.400E + 06	140

MIN = 5.805E + 05 58.05
MAX = 1.459E + 06 145.9

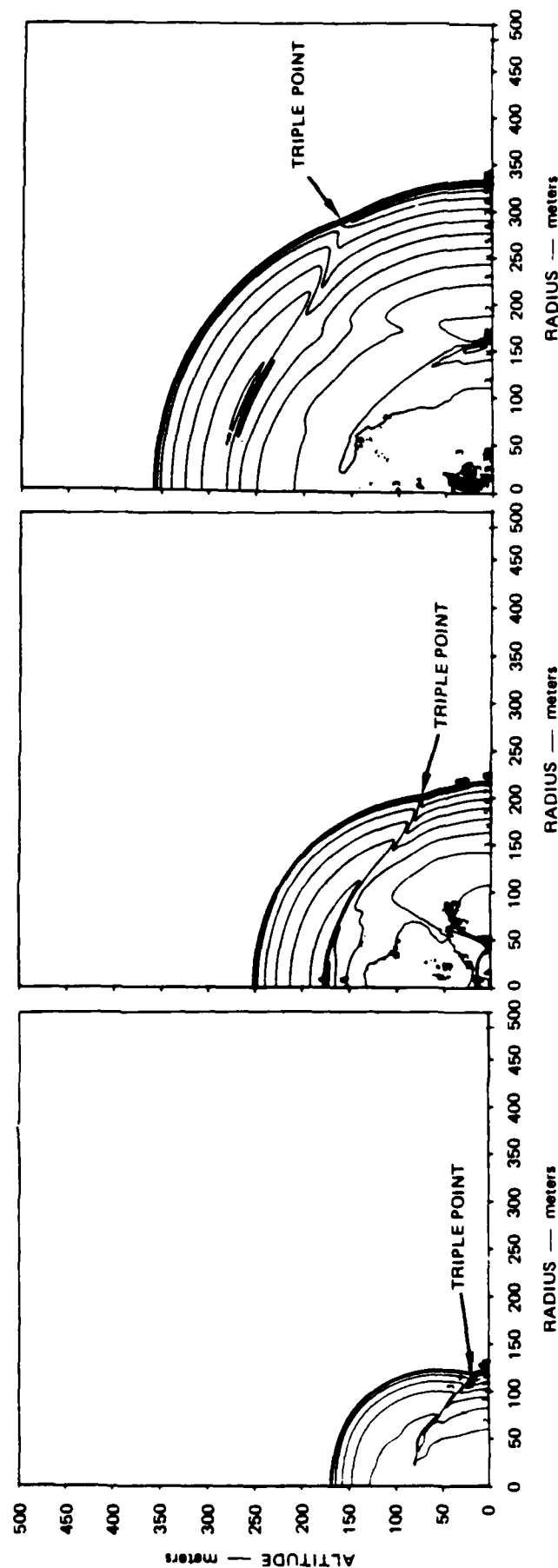


Figure 12. Results of HULL calculations for DIRECT COURSE pressure field at 100, 250, and 500 ms showing development of triple point.

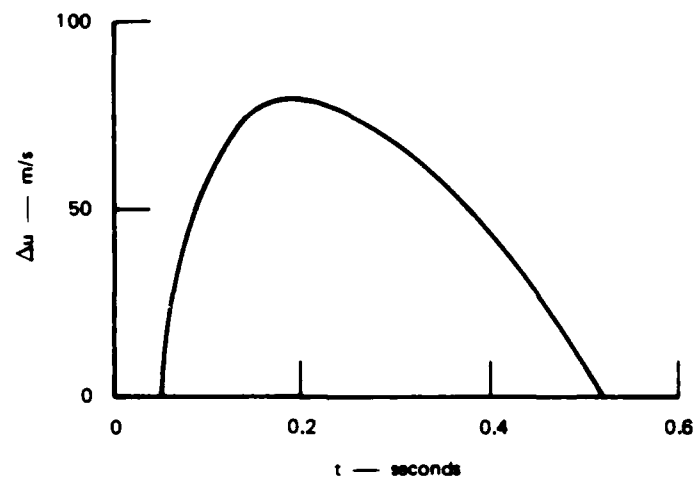


Figure 13. Velocity difference across triple-point slipstream.

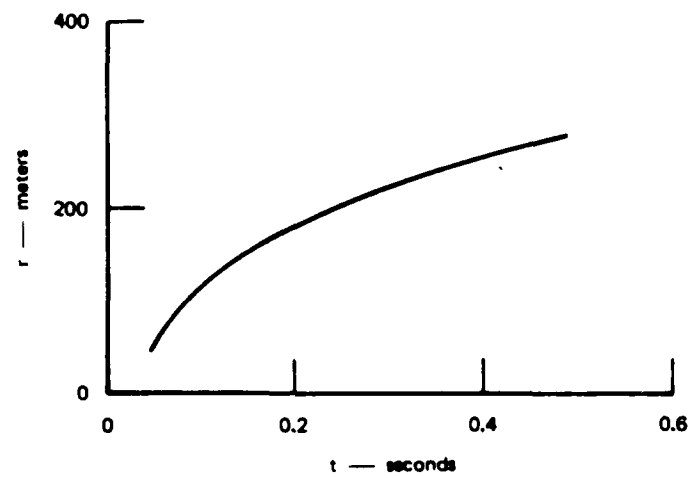


Figure 14. History of the triple-point radial location.

strong case is made for the triple point as the causative mechanism for ring-vortex formation, thereby providing the basis for the dust pedestal.

3.2.3 Mechanism for Dust-Pedestal Cellular Structure.

Two possible mechanisms to explain the observed cellular structure of the dust pedestal (Figure 15) were investigated, namely, convective (Benard) cell formation and ring-vortex instability. Benard cells form under conditions wherein a fluid is heated from below, causing a low-density region to form near the lower surface, giving rise to convective instability. HULL code calculations indicate that the flow near the ground is indeed unstably stratified (density increasing with distance from the ground), which would support the Benard-cell-type development. Benard convection, however, falls into three regimes--depending on the value of the Rayleigh number, which is defined by

$$Ra = \frac{g\beta\Delta T h^3}{\nu\alpha}, \quad (1)$$

where g is acceleration caused by gravity, β is the thermal expansion coefficient, ΔT is the temperature difference across the unstably stratified convective layer, h is the layer height, ν the kinematic viscosity, and α the thermal diffusivity. For $0 \leq Ra \leq 5600$, the convection is two-dimensional (no cellular structure). For $5600 \leq Ra \leq 12,000$, the flow is characterized by time-periodic three-dimensional disturbances, and for $Ra > 12,000$, more complex aperiodic spatial and temporal variations are observed. Indeed, for $Ra > 30,000$, the convection is sufficiently turbulent in appearance that well-defined thermal oscillations are rarely discernible. For the DIRECT COURSE event under consideration, a typical value of Rayleigh number based on a stratification-layer height of 30 m, a temperature difference across the layer (obtained from HULL calculations) of 220 °R, and values of β ,

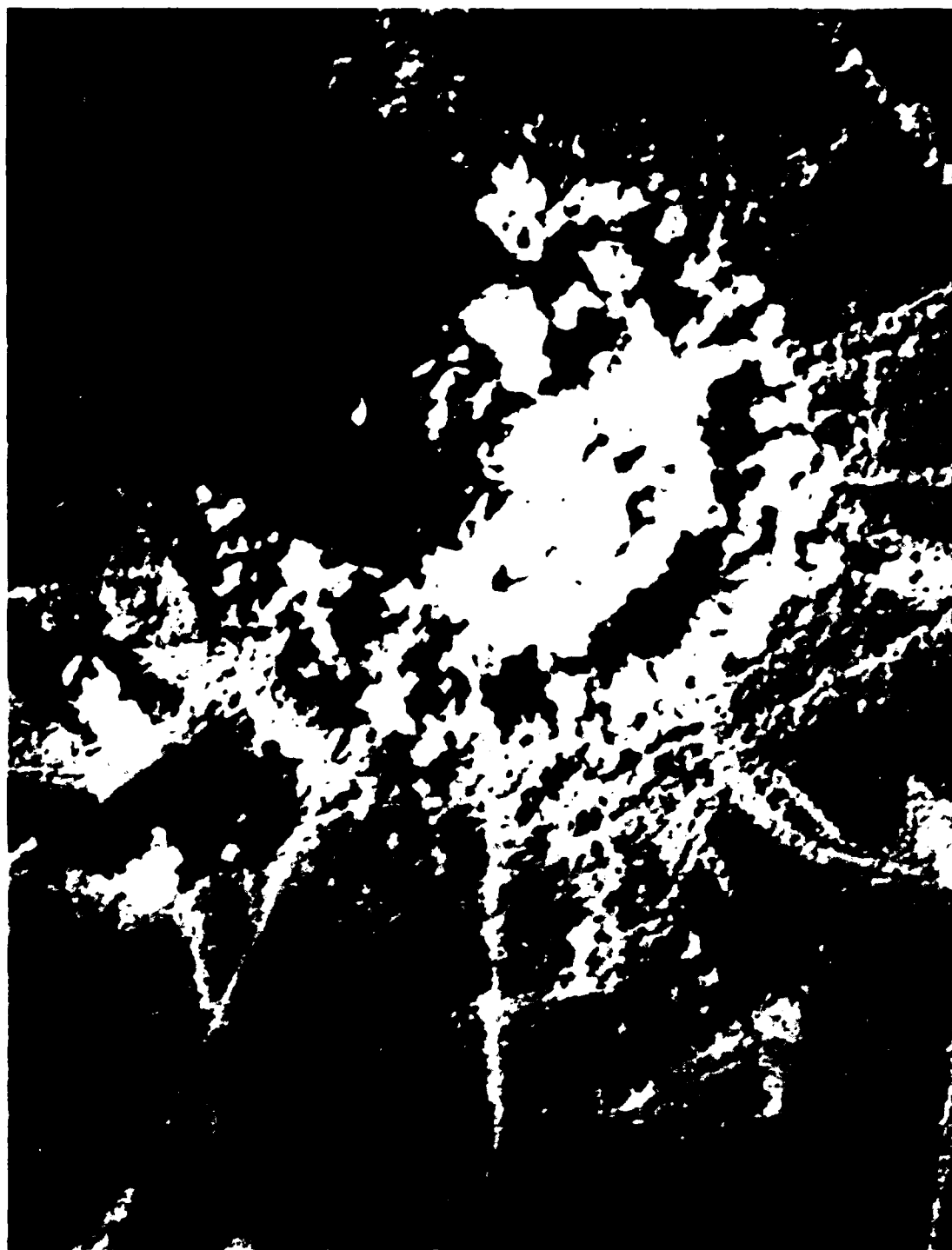


Figure 15. Overhead photograph of DIRECT COURSE event 4.5 s after detonation showing circumferential cellular structure of dust pedestal.

v , and α of $0.00204/^\circ R$, $8.1 \times 10^{-4} \text{ ft}^2/\text{s}$, and $8.3 \times 10^{-4} \text{ ft}^2/\text{s}$ respectively, is $Ra = 2 \times 10^{13}$, which is clearly in the turbulence aperiodic range, and thus would not be likely to display the regular circumferential cellular structure observed in the DIRECT COURSE event.

With regard to ring-vortex instability, the generating mechanism for formation of the ring vortex has already been identified in the above discussion concerning the triple point. Periodic waves may develop circumferentially around the ring vortex and have been experimentally observed (Figure 16). A theoretical analysis performed by Widnall and Sullivan² shows the number of unstable waves to be a function only of the ratio of the radius of the vortex core, a , to the radius of the vortex ring, R (Figure 17). The results of the analysis are shown in Figure 18, where n is the number of waves in the unstable mode and $\tilde{V} = \ln \frac{8R}{a} + C$, where C is a constant determined by the details of the swirl velocity distribution. (For example, if the velocity distribution is uniform, $C = -\frac{1}{4}$). The abscissa in Figure 18, \tilde{V} , is the ratio of the self-induced translational velocity of the vortex ring, V_0 , and the vortex strength, Γ , divided by twice the perimeter, $4\pi R$. For the 30 waves observed in the DIRECT COURSE event, extrapolation of the theoretical curve shown in Figure 18 results in $\tilde{V} \approx 5$ for $n = 30$, which, for a vortex-ring radius of 175 m, yields a core radius, a , of ~ 7.3 m. A more detailed estimate based on two-dimensional vortex-sheet rollup theory (cf. Section 3.2.3.2 below) yields a value of 15 m. The core of a vortex is defined as a region of constant angular velocity, ω , with tangential velocity varying as the radius according to $v = \omega r$, where $0 \leq r \leq a$ inside the core. Outside of the core, the tangential velocity varies as $1/r$.

3.2.3.1 Estimate of Vortex-Ring Parameters from Triple-Point Calculations.

A more-detailed estimate of vortex-ring parameters, including core size, can be made utilizing the triple-point data of Figures 11, 13, and



Figure 16. Ring-vortex periodic waves as generated in the laboratory by pulsing air through a sharp-edged orifice: (a) six waves and (b) seven waves.

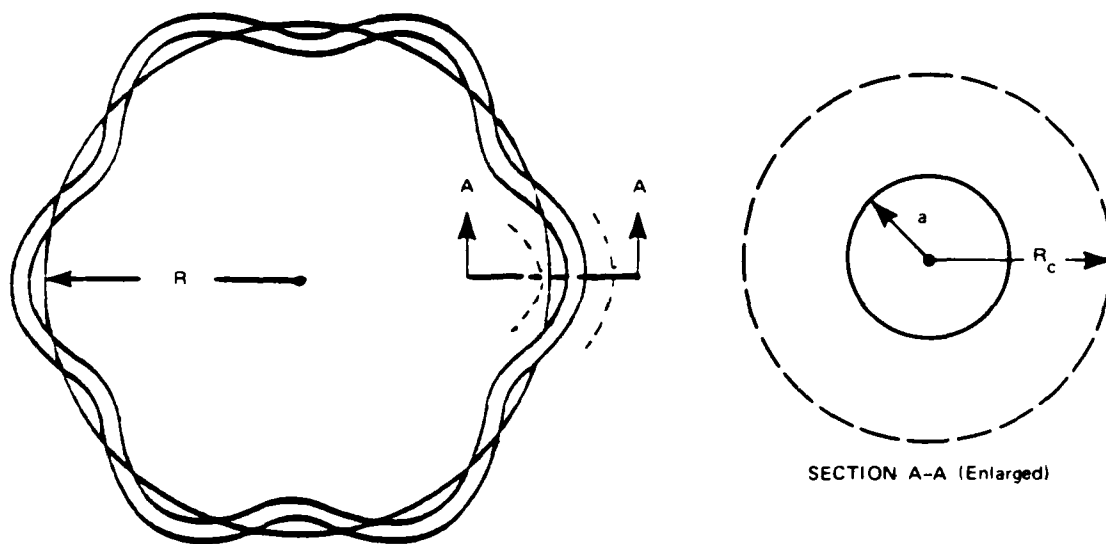


Figure 17. Ring-vortex nomenclature.

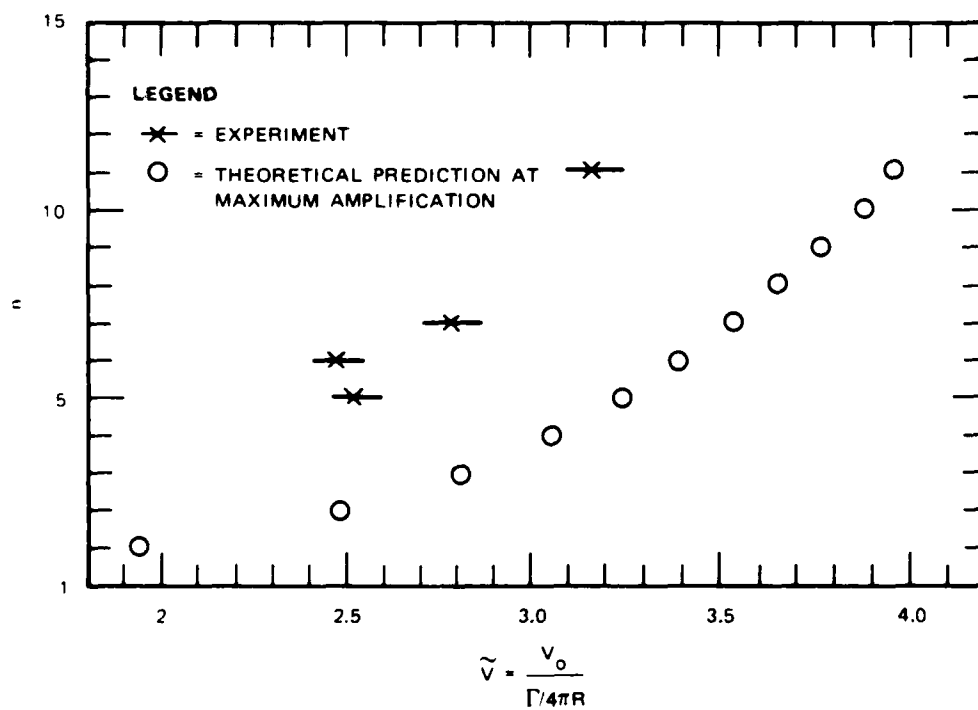


Figure 18. Results of vortex-ring circumferential stability analysis.

14. From the triple-point calculations of vortex sheet strength and vorticity distribution, it is possible to work out the properties of the vortex ring formed by the rollup of this sheet. Assuming that the time scale for ring rollup is much larger than the time scale for vortex-sheet formation caused by shock reflection, the initial ring radius is found by conserving the vertical impulse (or virtual momentum) in the vortex sheet. The effective core size of the resulting vortex ring is found by conserving kinetic energy. The total circulation is found by integrating the strength of the vortex sheet. The circulation and the effective core size, together with the ring radius, determine the self-induced motion of the ring toward the ground. The circulation and distance above the ground determine the velocity along the ground that the ring would have without the inflow accompanying the explosion. Estimates can then be made of the spatial wavelengths for the vortex-ring instability and the time scale over which it would occur.

To obtain an estimate of vortex properties, the numerical results for the strength of the vortex sheet vs. time, as well as the location of the triple point with time, were fit with simple mathematical functions so that the spatial distribution of vorticity $\gamma(r,y)$, where y is the vertical direction, could be obtained. From curve fitting to Figures 11, 13, and 14, it was determined that the formulae

$$h(r) = 20(r/100)^{1.9} \quad (2)$$

$$\gamma(t) = 300(t-0.05)(0.525-t)/t \quad (3)$$

and

$$r(t) = 325(t-0.045)^{1/3} \quad (4)$$

gave a reasonable fit to the numerical results consistent with the goals to provide a simple model of vortex behavior. With these formulae, $\gamma(r,y)$ was available, as well as the shape of the sheet, $h(r)$.

The geometric configuration of the initial vortex sheets is shown in Figure 19. The sheet begins at a radius of 55 m and extends to a radius of 255 m in meridional (h,r) planes. The height above the ground varies nonlinearly with r in Eq. (2); thus, the vortex sheet is not flat. To simplify the calculations, this sheet was assumed to be flat and to make an angle of 32 deg with the ground. The velocity difference across the sheet, Δu from Figure 13, was taken as the strength per unit length of the vortex sheet. The calculations were done in the r' coordinate system along the "flat" vortex sheet (see Figure 19).

3.2.3.2 Equivalent Core Size.

Calculations of the equivalent core size that result from the rollup of the vortex sheet are made by equating the kinetic energy in the sheet configuration to that of an equivalent vortex core of constant vorticity. This would give (for example) the correct core size to use if the self-induced velocity, v_i , of the ring were to be calculated by Kelvin's formula

$$v_i = \Gamma [\ln(8R/a) - 1/4] / 4\pi R \quad , \quad (5)$$

where Γ is the vortex strength, R the ring radius, and a the effective core size. This core size can also be used to give an estimate of the wavelength of the vortex-ring instability, although the calculation is not precise because the details of the vortex ring instability depend upon the actual distribution of the vorticity in the core³; this vortex sheet will not roll up to form a vortex of constant vorticity. These issues are discussed in Reference 4. The work of Widnall, et al⁵ shows that effective core size is determined from the kinetic-energy content of the flow in relation to an equivalent vortex of constant vorticity. The configuration for the calculation of kinetic energy is shown in

Figure 20. In general, the kinetic energy per unit mass of a flow containing a vortex sheet is given by

$$KE = -\int \Delta\phi v_n dS \quad , \quad (6)$$

where $\Delta\phi$ is the jump in velocity potential across a sheet, and v_n is the local velocity normal to the sheet. If the total vortex strength in the sheet, Γ , is not zero, the contour S must be taken to infinity because $\Delta\phi$ does not go to zero for such a flow at the edge of the sheet.

For a vortex core of constant vorticity, the kinetic energy of the vortex core must be included. Therefore, for the kinetic energy per unit mass of a vortex sheet we have

$$KE = -\int \Delta\phi v_n dr' \quad , \quad (7)$$

while for the kinetic energy per unit mass of a vortex core of constant vorticity we have

$$KE = -\int_a^\infty \Delta\phi v_n dr' + \frac{1}{2} \iint_A v_\theta^2 dA \quad , \quad (8)$$

where v_θ is the tangential velocity and A is the cross-sectional area of the vortex core. Because the potential jump across the sheet for an isolated vortex is constant and equal to $-\Gamma$, the integral may be evaluated analytically. For a core velocity of

$$v(r') = \Gamma r' / 2\pi a^2 \quad , \quad (9)$$

the contribution to the kinetic energy per unit mass from the core is

$$(KE)_{\text{core}} = \Gamma^2 / 16\pi \quad , \quad (10)$$

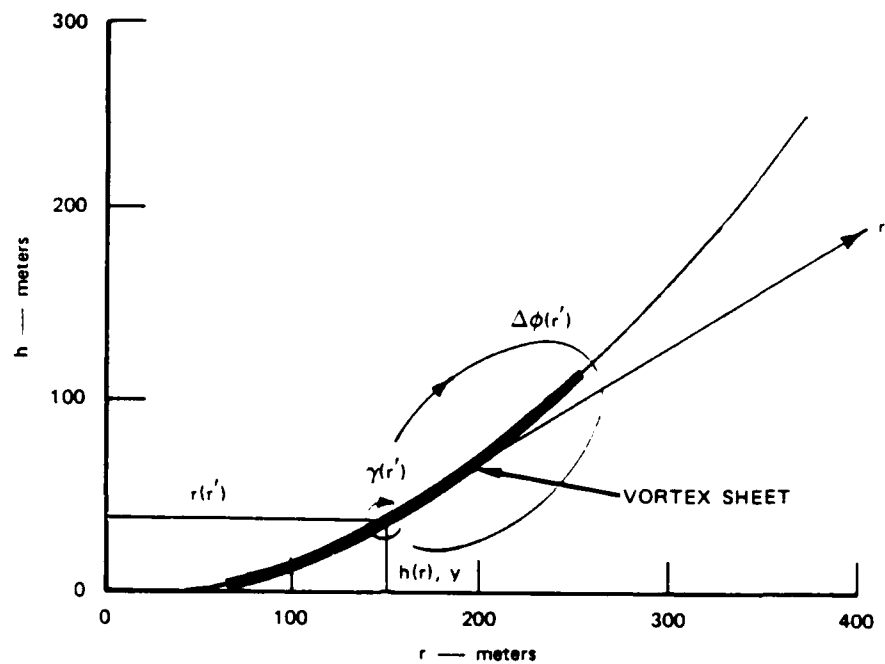


Figure 19. Coordinate system for vortex sheet calculations.

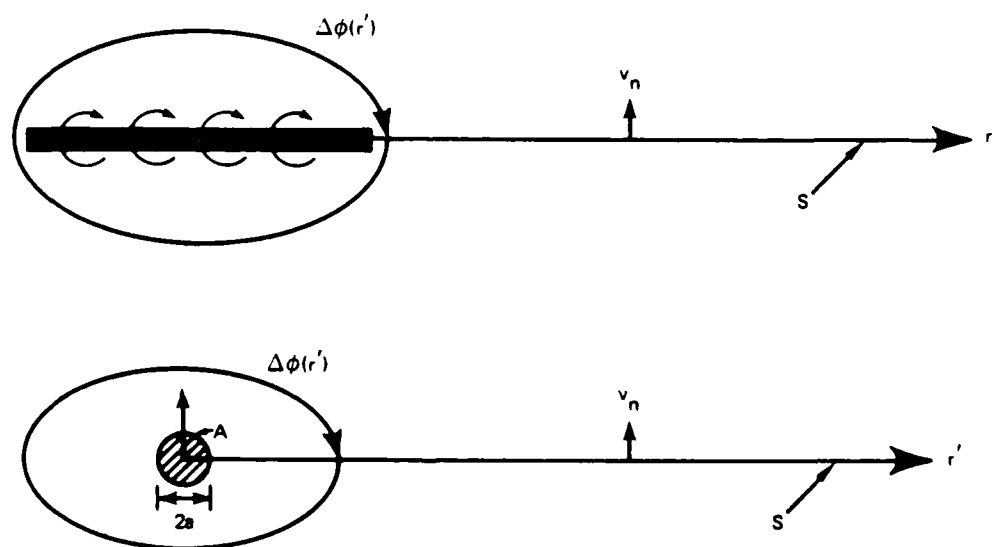


Figure 20. Equivalent core for vortex sheet rollup.

so that the total kinetic energy per unit mass of an isolated vortex core of constant vorticity is

$$KE = \lim_{r' \rightarrow \infty} \frac{1}{2} r'^2 (\ln r' - \ln a) / 4\pi + r'^2 / 16\pi \quad . \quad (11)$$

Note that this expression does not converge because $\ln r'$ continues to increase as $r' \rightarrow \infty$. However, the kinetic-energy integral for the vortex sheet also contains the same $\ln r'$ term; when the kinetic energy per unit mass of the two equivalent flows are equated these terms will cancel.

Equating the kinetic energy per unit mass from the vortex sheet to the kinetic energy per unit mass of an equivalent vortex core of constant vorticity gives, after some manipulation, an expression for the core size, a , of the form

$$\ln a = -[4\pi KE / \Gamma^2 - \ln r'] + 1/4 \quad . \quad (12)$$

We can now let $r' \rightarrow \infty$ and obtain a finite value for $\ln a$. Actually, the calculations were done numerically, and were terminated when the term in brackets reached a constant value. When this was done for the vortex sheet in question, values for the vortex-core size of $a = 42$ m and a circulation, Γ (where $\Gamma = \int_{\text{sheet}} \gamma dr'$), of about $9600 \text{ m}^2/\text{s}$ were obtained. This assumes that the vortex sheet was created near the ground and was allowed to roll up in its entirety without any other influences. It is clear, however, that the vortex sheet was subject to strong inflow from the flow rushing toward the axis. Therefore, it is unlikely that the entire vortex sheet was able to roll up as a unit. If we assume that only the 25-m extent of vortex sheet on either side of the vorticity maximum at $r = 175$ m rolls up as a single vortex, values of $a = 15$ m and vortex strength (circulation) of $4330 \text{ m}^2/\text{s}$ are obtained. Based on the DIRECT COURSE data, there is no way to accurately determine an experimental value of a . However, a value of 15 m compared with the overall effective vortex cross-sectional radius, R_c (Figure 17), of the

dust pedestal of about 25 m as determined from experimental data (e.g., Figure 15) appears reasonable.

When these parameters are used in the self-induced velocity formula, a vertical speed of 8.23 m/s is predicted, which is certainly compatible with the result shown in Figure 4 (HULL calculations) where the vortex is shown to have descended from an altitude of 50 m at $t = 1.5$ s to an altitude of 20 m at $t = 5$ s.

3.2.3.3 Stability Issues.

As discussed in Reference 3, the vortex-core instability depends upon the details of the distribution of vorticity. For constant vorticity, the wavenumber, k ($\equiv 2\pi/\lambda$, where λ is the wavelength) at which the instability will occur is given by $ka = 2.4$; for distributions that have a vorticity maximum at the center of the vortex, values of ka of 1.7 to 3.8 have been obtained.⁴ The experimental observations discussed here give an instability having 30 waves at a ring radius of about 180 m, yielding a value of $k = 30/180 \text{ m} = 0.167/\text{m}$. For a vortex core size of 15 m, this gives a value of ka of 2.5--very much in the expected range.

3.2.3.4 Amplification Rate.

An isolated vortex ring has a circumferential wave instability amplification rate proportional to $\Gamma/(4\pi R^2)$, which is proportional to the local strain caused by the ring flow field.⁶ However, the principal source of instability in the experimental situation comes from the vortex proximity to the ground; in this case, the vortex feels the strain field from its image, more like the short-wave vortex-pair instability.⁷ Thus, the amplification rate will be proportional to $\Gamma/[2\pi(4h^2)]$ because the vortex is located a distance $2h$ from its image. Estimating the height of the vortex at 20 m above the ground gives an amplification rate, α , of 0.43 s^{-1} . Experimental observations² suggest that the instability is complete at about $\alpha t = 2$, or at a time of about

4 s after vortex formation is complete. Short-wave vortex instabilities, whether caused by the strain field of the ring or by the proximity to the ground, occur at the same wavenumber, namely that of the critical second bending mode as discussed in Reference 3. For the DIRECT COURSE event, HULL calculations show the vortex to be completely formed at about 1 s (Figure 4) and the overhead photograph of Figure 15 shows the circumferential cellular structure to be completely formed by about 4.5 s, thereby substantially agreeing with the laboratory results of Reference 2.

3.2.3.5 Impulse--Initial Ring Radius.

The vortex rollup method can also be applied to determine the initial radius of the ring. This requires that we ignore both the influence of the ground and the strong inflow upon the rollup. A vortex sheet rolling up conserves its impulse or virtual momentum. The impulse of a circular vortex sheet is

$$I = 2\pi \int \Delta\phi \, r \, dr' \quad (13)$$

(see Figure 19) for definitions. For this ring, we require that the initial impulse equal the final impulse of the rolled-up ring, which is simply

$$I = \Gamma \pi R^2 \quad , \quad (14)$$

where R is the final radius of the ring. Integrating the impulse of the vortex sheet, equating it to the impulse of the ring in its final configuration, and solving for R gives $R = 161$ m, which is in reasonable agreement with the HULL calculations that show a vortex at a radius $r = 180$ m.

3.2.3.6 Interpretation of HULL Calculations in Terms of a Vortex Model.

The vortex model presented here is somewhat idealized in comparison with the complexity of the flow predicted by the HULL calculations and shown in Figure 4; it cannot be expected to predict all of the observed phenomena. Nevertheless, it seems to have the predictive power to explain features of both HULL calculations and experiments. Additional observations can be made about the numerical results based on vortex modeling. First, the time from $t = 1$ to 5 s seems to be a time of vortex rollup. However, the vortex sheet is subject to a strong inflow toward the axis, which is not in the simple model and may affect the portion of the vortex sheet that forms the concentrated core. The period from $t = 5$ to $t = 10$ s seems to be a period of vortex motion and instability. If the vortex were isolated in the presence of the ground plane, it would move out along the wall at a velocity given by

$$v_{\text{ground}} = \Gamma / (4\pi h) \quad (15)$$

or at about 17 m/s. That the vortex remains stationary at $r = 180$ m, from $t = 5$ to $t = 15$ s, means that the inflow must have a value close to this, because the vortex is convected by the combination of self-induced and inflow velocity.

3.2.3.7 Direct Calculations of Vortex Sheet Rollup.

A direct simulation of the rollup of the vortex sheet created by the triple-point shock reflection can be used to verify the model of the previous section and to compare with the HULL calculations. To obtain a simple model, a local two-dimensional vortex sheet was used. This model does not include the self-induced motion caused by curvature, but it should be accurate for a preliminary investigation. The effect of proximity to the ground is included through a system of images. Since

the velocity field associated with the curvature of the vortex ring is not included, and this is negative at the vortex sheet, the height of the sheet above the ground will be overestimated.

The vortex sheet is represented by a number of discrete vortex elements; in this case, 100 elements were used. The velocity of each element is given by the influence of the other vortices including the images. The effect of inflow toward the axis is included by adding a negative horizontal velocity of 15 m/s to each vortex element. (This value was chosen somewhat arbitrarily; therefore, the value of r at which the vortex sheet is found is not accurate in time.) The vortex points are moved in time with this combined velocity. Proceeding in time produces a simulation of the behavior of the vortex sheet.

If the vortex sheet is represented as a set of point vortices of strength, γ_i , located at the point, (r_i, y_i) , the velocity components in the r, y directions of each point are given by

$$\frac{dr_i}{dt} = - \frac{1}{2\pi} \sum_j \gamma_j \left[\frac{y_i - y_j}{(y_i - y_j)^2 + (|r_i - r_j| + dr)^2} - \frac{y_i + y_j}{(y_i + y_j)^2 + (|r_i - r_j| + dr)^2} \right] \quad (16)$$

$$\frac{dy_i}{dt} = \frac{1}{2\pi} \sum_j \gamma_j (r_i - r_j) \left[\frac{1}{(y_i - y_j)^2 + (|r_i - r_j| + dr)^2} - \frac{1}{(y_i + y_j)^2 + (|r_i - r_j| + dr)^2} \right] \quad (17)$$

where dr is a convergence factor that can be interpreted as an effective core diameter for the vortex element; this is a standard technique in vortex methods to avoid chaotic behavior.

Equations (16) and (17) were integrated numerically from $t = 0$ to $t = 8$ s. The results are shown in Figures 21 to 26. Figures 21, 22, and 23 show the position of the vortex sheet as a function of time; $t = 0$ corresponds to the initial vortex sheet position; the position of the sheet at subsequent times is also shown. The formation of a vortex is noticeable at $t = 3$ s. One interesting feature of the rollup of this vortex sheet is the strong interaction with the ground. The vorticity that rolls up to form the vortex comes from the left edge of the original vortex sheet after its strong interaction with the ground. The central portion of the sheet does not roll up into the vortex within 8 s. The calculations break down after some time in the region of the vortex core; more sophisticated calculations would need to be done to overcome these difficulties.

The velocity field from this vortex sheet is shown in Figures 24, 25, and 26 at $t = 0, 3$, and 8 s. The shape of the vortex sheet is also shown in these figures. Recall from Figures 13 and 14 that the maximum of the vorticity occurs at about $r = 175$ m. This results in a strong vortex flow even when the sheet is not formed. At later times, the concentrated vortex rollup becomes a center of vorticity.

3.2.3.8 Conclusions.

These vortex sheet calculations demonstrate the process of rollup that forms the concentrated vortex from the initial vortex sheet caused by the triple-point shock reflection. Although not all of the observed features of the flow field are reproduced in these simple calculations (because several important flow-field features were not included in the model), one important feature is clear: not all of the vortex sheet is

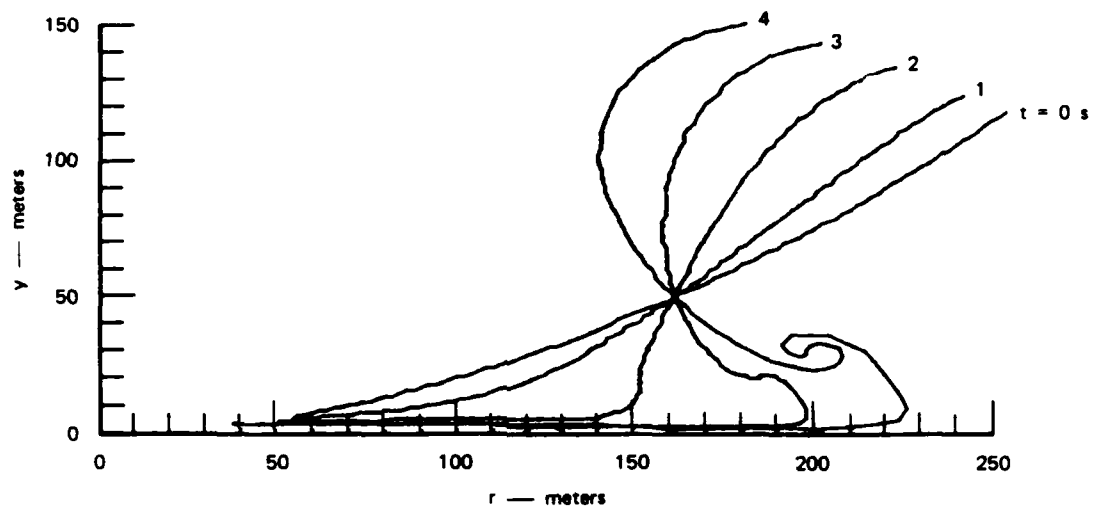


Figure 21. Calculated vortex position as function of time, $t = 0$ to 4 s.

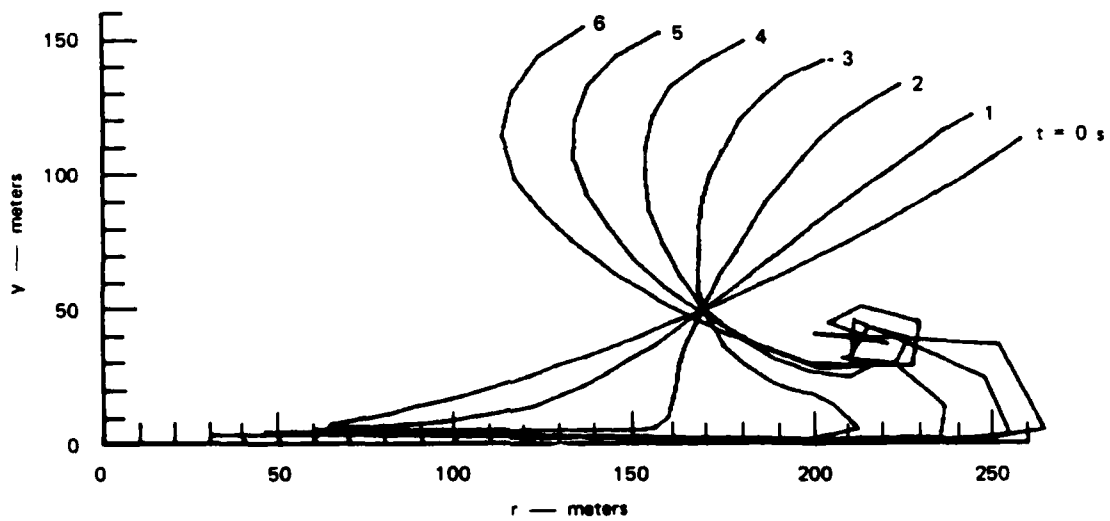


Figure 22. Calculated vortex position as function of time, $t = 0$ to 6 s.

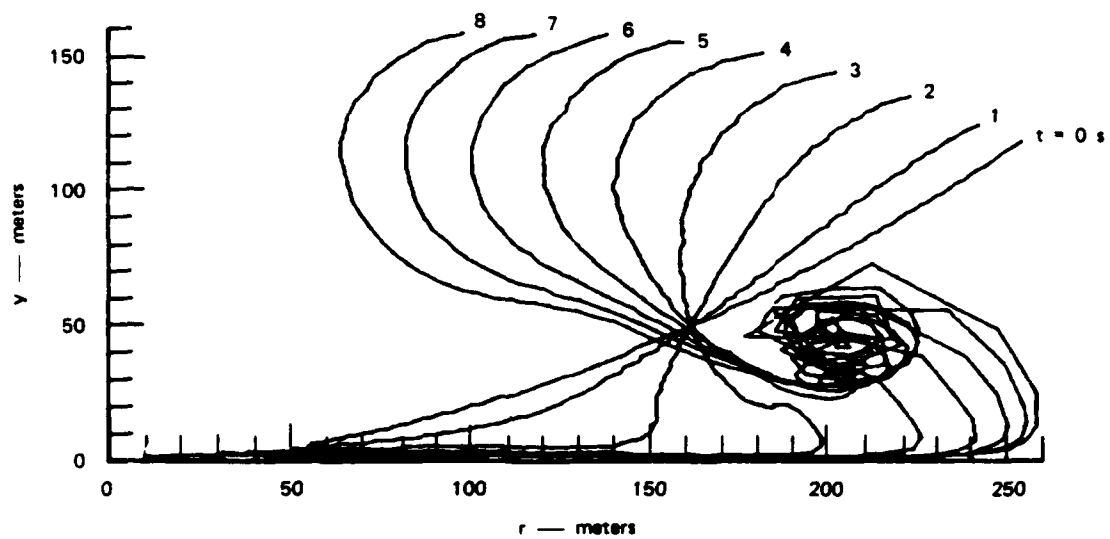


Figure 23. Calculated vortex position as function of time, $t = 0$ to 8 s.

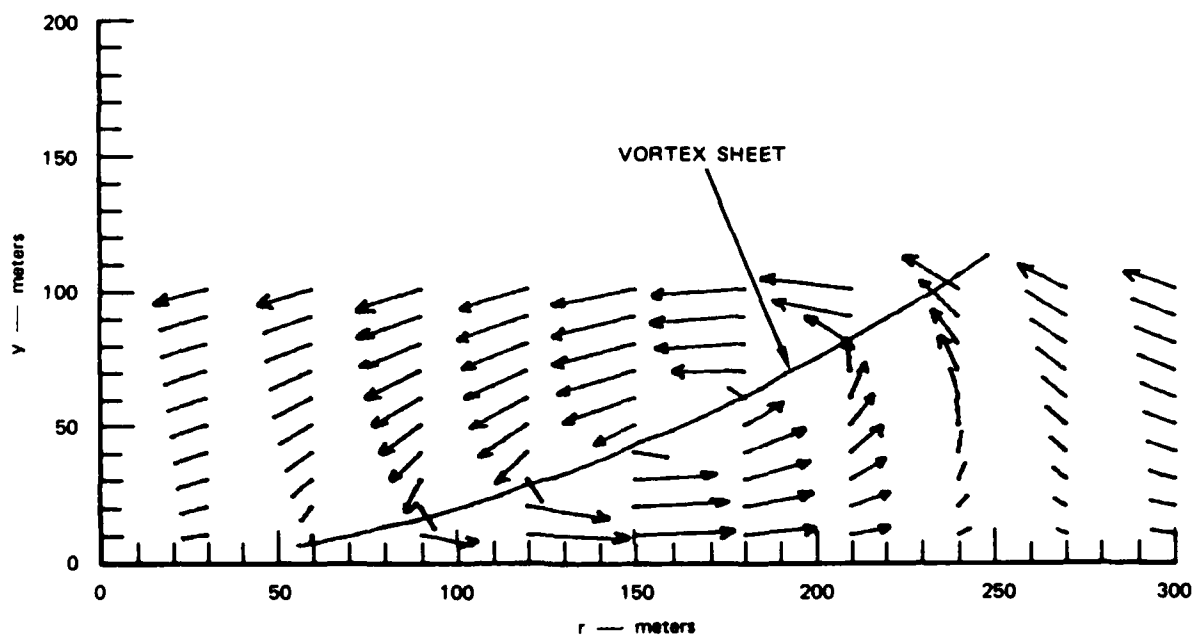


Figure 24. Vortex sheet velocity field, $t = 0$ s.

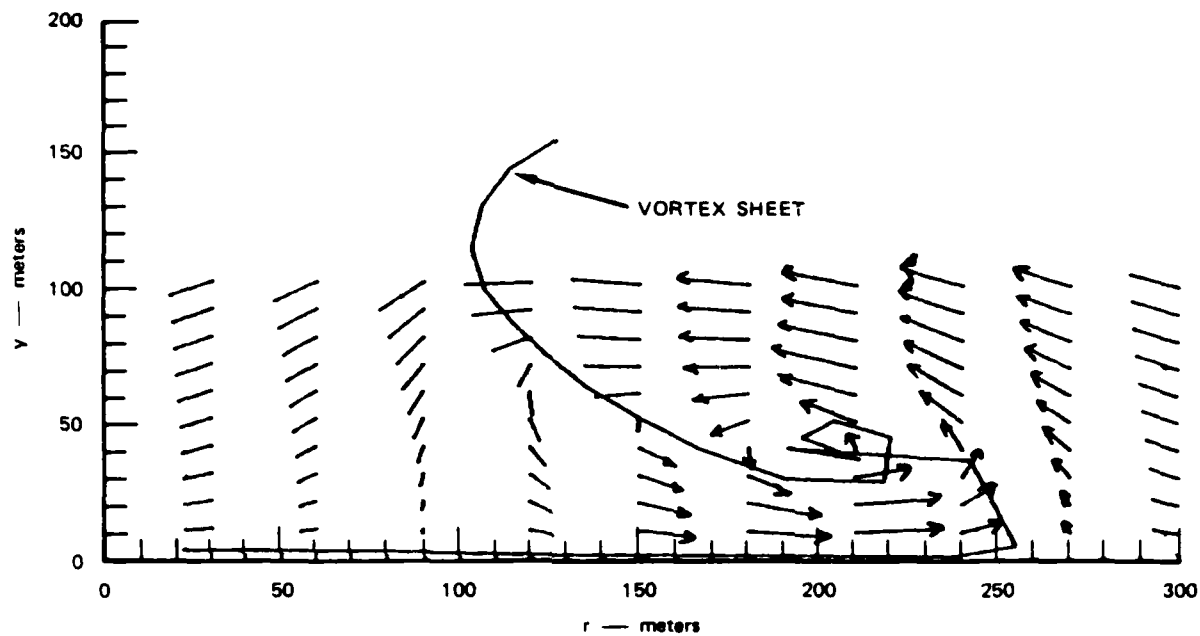


Figure 25. Vortex sheet velocity field, $t = 3$ s.

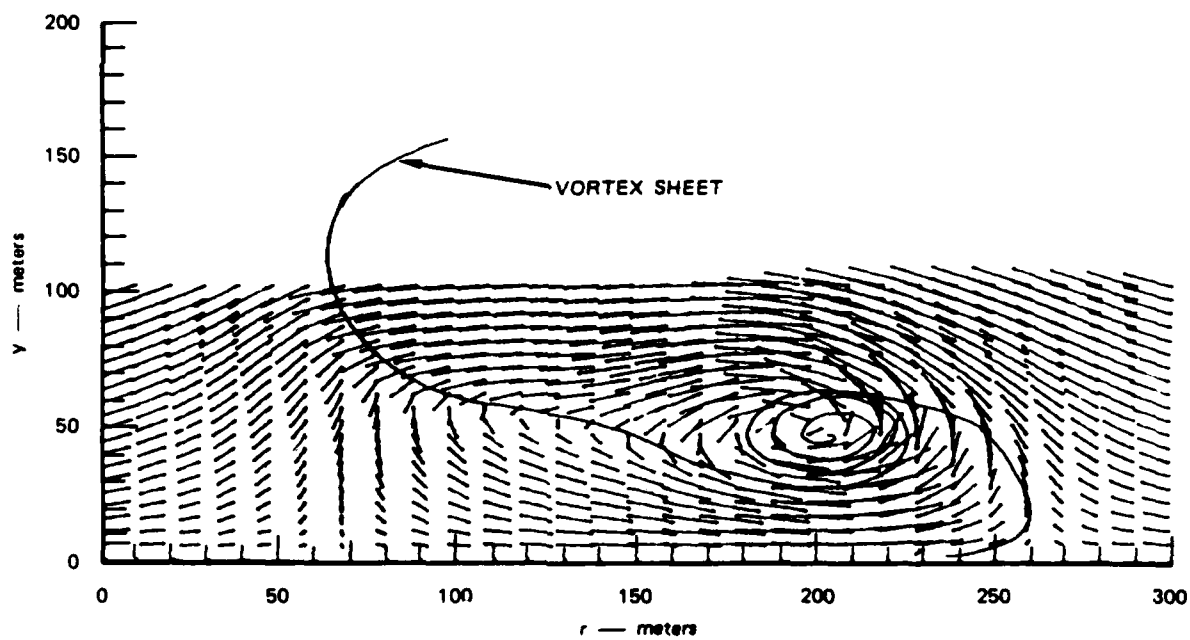


Figure 26. Vortex sheet velocity field, $t = 8$ s.

rolled up to form the concentrated core near the ground. Therefore, its circulation will not be the circulation of the initial sheet, and its core size will be only a fraction of the core size that would result from rollup of the entire sheet. More detailed calculations could be done to overcome the limitations of two-dimensional flow and to incorporate numerical techniques that would allow the rollup to be followed for longer times.

Thus, when one considers both the Benard convective-cell phenomenon and vortex-sheet rollup with vortex-ring instability, the latter phenomenon appear to be the most likely explanation for the observed DIRECT COURSE dust pedestal and its ring-wave cellular structure.

SECTION 4

LIST OF REFERENCES

1. White, D. R., "An Experimental Survey of the Mach Reflection of Shock Waves," Proc. Midwestern Cont. on Fluid Mechanics (1952).
2. Widnall, S. E. and J. P. Sullivan, "On the Stability of Vortex Rings," Proceedings of the Royal Society of London, A332, pp. 335-353 (1973).
3. Widnall, S. E., D. B. Gliss, and C. Y. Tsai, "The Instability of Short Waves of Vortex Rings," J. Fluid Mech., Vol. 66, pp. 35-47 (1974).
4. Widnall, S. E., "Three-Dimensional Instability of Vortices in Separated Flows," Proceedings of the International Symposium on Separation Flows, Norway Institute of Technology, Trondheim, Norway (1985).
5. Widnall, S. E., D. B. Bliss, and A. Zalay, "Theoretical and Experimental Studies of the Stability of a Vortex Pair," Proceedings of the BSRL/AFOSR Symposium on Aircraft Wake Turbulence, Plenum Press (1971).
6. Widnall, S. E. and C. Y. Tsai, "The Instability of the Thin Vortex Ring of Constant Vorticity," Phil. Trans. of the Royal Society of London, Vol. 287, No. 1344, pp. 273-305 (1977).
7. Tsai, C. Y. and S. E. Widnall, "The Stability of Short Waves on a Vortex Filament in a Weak Externally Imposed Strain Field," J. Fluid Mech., Vol. 73, pp. 721-733 (1976).

DISTRIBUTION LIST

DEPARTMENT OF DEFENSE

ASSISTANT TO THE SECRETARY OF DEFENSE
ATOMIC ENERGY
ATTN: EXECUTIVE ASSISTANT

DEF RSCH & ENGRG
ATTN: STRAT & SPACE SYS (OS)

DEFENSE INTELLIGENCE AGENCY
ATTN: DB-4D
ATTN: DT-2
ATTN: DT-2 T DORR
ATTN: RTS-2B

DEFENSE NUCLEAR AGENCY
ATTN: NASF
ATTN: OPNA
3 CYS ATTN: SPWE
4 CYS ATTN: TITL

DEFENSE TECHNICAL INFORMATION CENTER
12 CYS ATTN: DD

FIELD COMMAND DEFENSE NUCLEAR AGENCY
ATTN: FCTXE
ATTN: FTTD
ATTN: FTTD W SUMMA

FIELD COMMAND/DNA
ATTN: FC-1

JOINT CHIEFS OF STAFF
ATTN: J-5 NUCLEAR & CHEMICAL DIV
ATTN: JAD/SFD
ATTN: JAD/SSD

JOINT STRAT TGT PLANNING STAFF
ATTN: JK (ATTN: DNA REP)
ATTN: JKCS

DEPARTMENT OF THE ARMY

HARRY DIAMOND LABORATORIES
ATTN: SCHLD-NW-P

U S ARMY MATERIAL TECHNOLOGY LABORATORY
ATTN: DRXMR-HH J DIGNAM

U S ARMY MISSILE COMMAND
ATTN: AMSMI-RD-UB H GREENE

U S ARMY NUCLEAR & CHEMICAL AGENCY
ATTN: LIBRARY

U S ARMY TRADOC SYS ANALYSIS ACTVY
ATTN: ATAA-TDC R BENSON

DEPARTMENT OF THE NAVY

NAVAL RESEARCH LABORATORY
ATTN: CODE 4650 A WILLIAMS

NAVAL WEAPONS EVALUATION FACILITY
ATTN: CLASSIFIED LIBRARY

OFC OF THE DEPUTY CHIEF OF NAVAL OPS
ATTN: OP 654(STRAT EVAL & ANAL BR)

STRATEGIC SYSTEMS PROGRAM OFFICE (PM-1)
ATTN: NSP-2722
ATTN: NSP-273

DEPARTMENT OF THE AIR FORCE

AERONAUTICAL SYSTEMS DIVISION
ATTN: ASD/ENSSS H GRIFFIS

AIR FORCE SYSTEMS COMMAND
ATTN: SDM

AIR FORCE TECHNICAL APPLICATIONS CTR
ATTN: TX

AIR FORCE WEAPONS LABORATORY, NTAAB
ATTN: NTES
ATTN: SUL

AIR FORCE WRIGHT AERONAUTICAL LAB
ATTN: AFWAL MLBT W ANSPACH

AIR UNIVERSITY LIBRARY
ATTN: AUL-LSE

BALLISTIC MISSILE OFFICE/DAA
ATTN: ENS
ATTN: ENSN
ATTN: MYE

DEPUTY CHIEF OF STAFF/AF-RDQM
ATTN: AF/RDQI

HQ USAF/XOXFS
ATTN: AFXOOTS

STRATEGIC AIR COMMAND/NRI-STINFO
ATTN: NRI/STINFO

DNA-TR-86-352-REV (DL CONTINUED)

DEPARTMENT OF ENERGY

LOS ALAMOS NATIONAL LABORATORY
ATTN: S S HECKER

OTHER GOVERNMENT

CENTRAL INTELLIGENCE AGENCY
ATTN: OSWR/NED

DEPARTMENT OF DEFENSE CONTRACTORS

ACUREX CORP
ATTN: C WOLF

AEROJET GENERAL CORP
ATTN: A COLLINS

AEROSPACE CORP
ATTN: H BLAES

APTEK, INC
ATTN: T MEAGHER

AVCO CORPORATION
ATTN: A PALLONE
ATTN: W REINECKE

BOEING CO
ATTN: A DACOSTA

BOEING MILITARY AIRPLANE CO
ATTN: D SAWDY

CALIFORNIA RESEARCH & TECHNOLOGY, INC
ATTN: K KREYENHAGEN
ATTN: M ROSENBLATT

CALSPAN CORP
ATTN: M DUNN

CARPENTER RESEARCH CORP
ATTN: H J CARPENTER

G B LABORATORY, INC
ATTN: G BURGHART

GENERAL ELECTRIC CO
ATTN: A GARBER
ATTN: B MAGUIRE

H-TECH LABS, INC
ATTN: B HARTENBAUM

HAROLD ROSENBAUM ASSOCIATES, INC
ATTN: G WEBER

HERCULES, INC
ATTN: P MCALLISTER

KAMAN SCIENCES CORP
ATTN: L MENTE
ATTN: R RUETENIK
ATTN: W LEE

KAMAN SCIENCES CORP
ATTN: J HARPER

KAMAN TEMPO
ATTN: B GAMBILL
ATTN: DASIAC

KAMAN TEMPO
ATTN: DASIAC

MARTIN MARIETTA DENVER AEROSPACE
ATTN: E STRAUSS

MCDONNELL DOUGLAS CORP
ATTN: D JOHNSON
ATTN: L COHEN

MCDONNELL DOUGLAS CORP
ATTN: M POTTER

MORTON THIOKOL, INC
ATTN: J HINCHMAN
ATTN: K HESS

PACIFIC-SIERRA RESEARCH CORP
ATTN: H BRODE, CHAIRMAN SAGE

PHYSICS INTERNATIONAL CO
ATTN: J SHEA

R & D ASSOCIATES
ATTN: F A FIELD
ATTN: P RAUSCH

RAND CORP
ATTN: P DAVIS

RAND CORP
ATTN: B BENNETT

S-CUBED
ATTN: G GURTMAN

SCIENCE APPLICATIONS INTL CORP
ATTN: J STODDARD

SCIENCE APPLICATIONS INTL CORP
ATTN: J COCKAYNE
ATTN: W LAYSON

SRI INTERNATIONAL
2 CYS ATTN: D MCDANIEL

TECHNOLOGY DEVELOPMENT ASSOCIATES
ATTN: C HARRELL
ATTN: N DISPENSIERE

TITAN SYSTEMS, INC
ATTN: P C DAVENPORT

TOYON RESEARCH CORP
ATTN: J CUNNINGHAM

TRW ELECTRONICS & DEFENSE SECTOR
ATTN: A ZIMMERMAN

TRW ELECTRONICS & DEFENSE SECTOR
ATTN: D GLENN
ATTN: N GUILLES
ATTN: W POLICH

Dist-4

END

DATE

FILMED

JAN

1988